ELASTIC MATERIAL PROPERTIES OF FRICTION STIR WELDED JOINTS IN STEEL

Digital Image Correlation
Measurements, Algorithms and Data Analysis

Yuyuan Chen

Marine Technology
Mechanical, Maritime and Materials Engineering Faculty
Delft University of Technology

October 2023

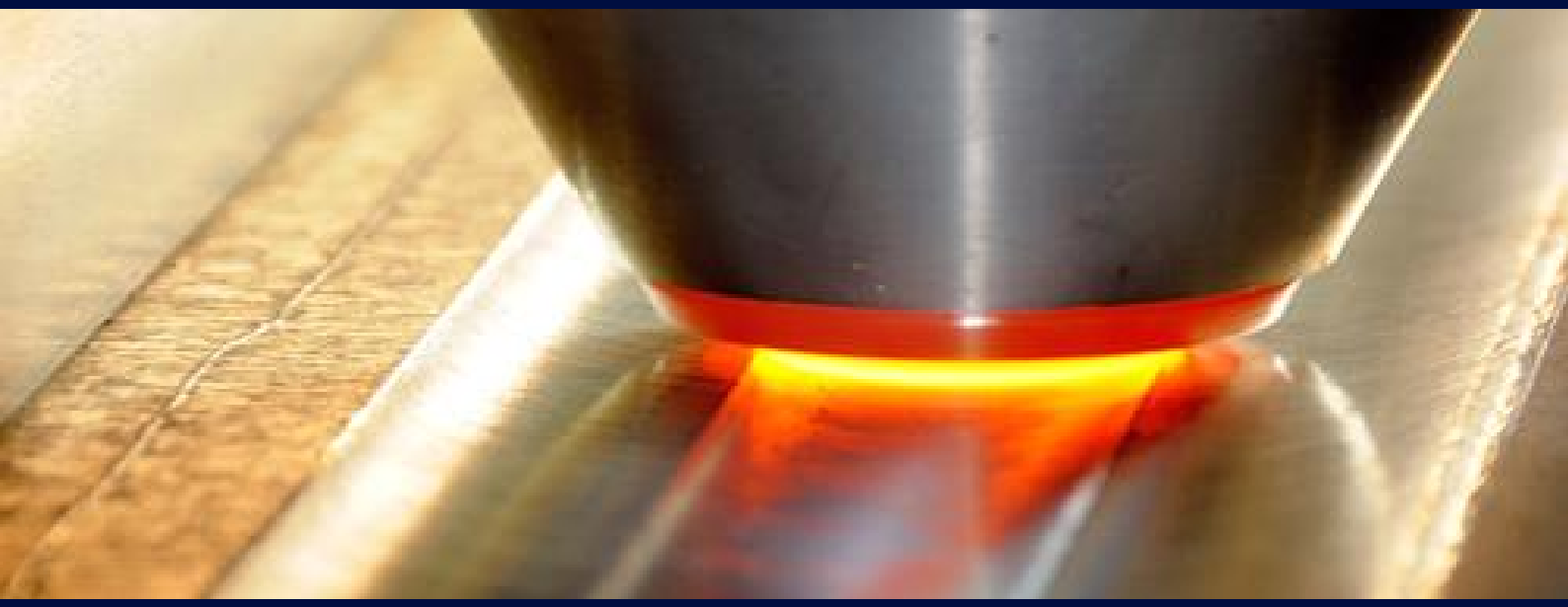

TU Delft

ELASTIC MATERIAL PROPERTIES OF FRICTION STIR WELDED JOINTS IN STEEL

Digital Image Correlation Measurements, Algorithms and Data Analysis

by

Yuyuan Chen

to obtain the degree of Master of Science
at the Delft University of Technology,

Student number:	5465532	
Report number:	MT.23/24.001.M	
Project duration:	December, 2022 – September, 2023	
Thesis committee:	Dr. ir. J. H. den Besten,	TU Delft, supervisor
	ir. Niels Troost,	TU Delft, supervisor
	Dr. Apostolos Grammatikopoulos,	TU Delft, committee member

TU Delft

Abstract

With the growing demand for high productivity and fabrication efficiency in building marine structures at European shipyards, the Robotic Survey, Repair and Agile Manufacture (RESURGAM) H2020 project has been initiated. The aim is to develop Friction Stir Welding (FSW) for the industry: an efficient solid-state joining process. Originally developed for the welding of aluminum and magnesium, FSW involves a fast-rotating tool being pushed into the material, moving along the interface of the structural members to be joined. The rotating tool introduces friction-induced heat to soften and mix the material in order to establish a joint. Given the many technical, environmental, and economic advantages of the FSW process, the aim is to introduce the process to the welding of steel. However, FSW locally modifies the material, introducing different zones, meaning the distribution of local mechanical properties like the Youngs modulus E is highly inhomogeneous and may vary from one location to another. In order to establish the distribution, a field measurement technique like Digital Image Correlation (DIC) can be adopted. This thesis has aimed to obtain distinguished elastic material properties for the parent material and nugget material zone, including the most likely transition boundaries using DIC. First, Texture quality analysis was implemented to determine the feasible subset size. Following the experiment and simulation setup 2D DIC algorithms like Augmented Lagrangian DIC (ALDIC) and Reliability-Guided Digital Image Correlation (RG-DIC) have been compared for formulation performance evaluation and practical measurement in a further stage. For the comparison reference, the unfiltered measurement results from global DIC algorithm Correli and results from 2D FEM analysis were employed. A Brutal Force method was adopted in order to identify the weld nugget zone boundary lines. Finally, the local elastic mechanical property parameters like Young's Modulus and Poisson's Ratio were calculated for the specified material region. And conclusions were made that plastic material properties would have appeared under the load level of $400MPa$. Future outlooks based on the research results and failures were discussed in the last chapter.

Keywords: Friction Stir Welding, Digital Image Correlation, Local Elastic Mechanical Properties

Acknowledgements

First I would like to express my sincere appreciation to my supervisor, Dr. ir. J.H. den Besten. His unwavering commitment to rigorous and meticulous guidance has been invaluable throughout my research period. Furthermore, he has shown great consideration for my personal development, offering valuable insights and creating opportunities for my career planning.

I am also deeply grateful to my co-supervisor, ir. Niels Troost. His extensive knowledge and experience in Digital Image Correlation (DIC) and Friction Stir Welding (FSW) have been instrumental in providing me with practical and professional advice, both in the realms of literature writing and experimental skills. In the initial stages, my proficiency in Matlab was insufficient for independent data processing and debugging, and ir. Troost generously dedicated his time to provide me with practical guidance. With their coordinated support, I am proud to say that I have significantly improved my skills and am well-prepared to embark on my engineering career.

I extend my heartfelt thanks to Dr. Apostolos Grammatikoupolos, a committee member who played a pivotal role in accommodating my accelerated thesis schedule. His recognition of my work was pivotal in making this endeavor possible, and his critical feedback during the green light meeting was instrumental in refining my thesis work.

I am also indebted to my seniors who have supported me during challenging technical moments. As an international student living independently abroad, their assistance extended beyond my master's thesis, encompassing all aspects of my academic, professional, and personal life.

Lastly, I want to convey my deepest gratitude to my parents. Their unwavering financial and emotional support has provided me with the invaluable opportunity to complete this Master's program in the Netherlands. They have shouldered responsibilities and pressures beyond my imagination and have given me the courage to remain true to myself. I am thankful to everyone who has offered me encouragement and love over the course of these two years, and I will treasure these cherished memories throughout my lifetime.

Yuyuan Chen

Contents

List of Figures

List of Tables

Acronyms

ADMM Alternating Direciton Method of Multipliers

AIN Average Iteration Number

ALDIC Augmented Lagrangian DIC

BA Bundle Adjustment

BMZ Base Material Zone

CB Confidence Bound

CCD Charged-Coupled Device

DA Diffuse Approximation

DIC Digital Image Correlation

DLT Direct Linear Transformation

FDM Finite Difference Method

FEM Finite Element Method

FVM Finite Volume Method

FSW Friction Stir Welding

HAZ Heat Affected Zone

IC-GN Inverse Compositional Gauss-Newton method

IHFESM Improved Hermite Finite Element Smoothing Method

ILS Iterative Least Square algorithm

ISP Integrally Stiffened Panel

LSM Least-Square Matching

MLE Maximum Likelihood Estimator

NCC Normalised Cross-Correlation

NR Newton-Raphson method

PLS Pointwise Least Square algorithm

RESURGAM Robotic Survey, Repair and Agile Manufacture

RG-DIC Reliability-Guided Digital Image Correlation

RGDT Reliability-Guided Displacement Tracking

RMS Root Mean Square

ROI Region Of Interest

SD Standard Deviation

SDE Standard Deviation Errors

SSD Sum of Squared Differences

STD Standard Deviation

TMAZ Thermal-mechanically Affected Zone

TWI The Welding Institute

UFSW Underwater Friction Stir Welding

UTS Ultimate Tensile Strength

WNZ Weld Nugget Zone

ZNCC Zero-mean Normalized Cross Correlation

ZNSSD Zero-Normalized Sum of Squared Differences

1 Introduction

1.1. Motivation

Conventionally, welding was defined as a heat fabrication process that joints different types of materials together. Friction Stir Welding(FSW), as a representative technique of solid state welding, originally invented by The Welding Institute (TWI) in 1991[1], is growing in popularity among the industry for its superiority in material mechanical properties and automation.

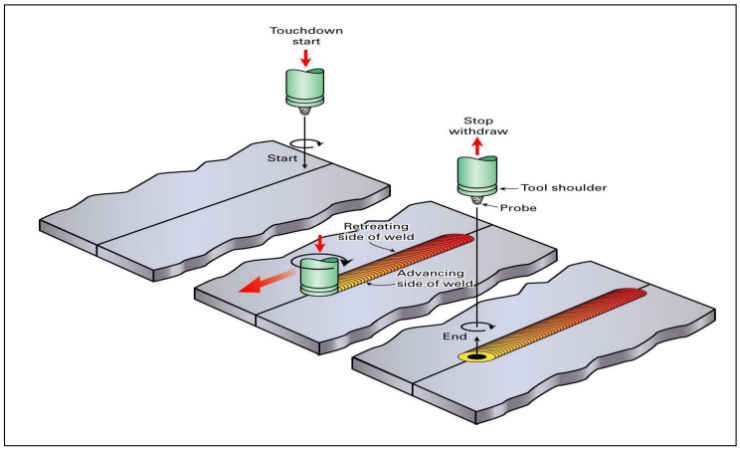

Figure 1.1: Schematic of Friction Stir Welding process[2]

Due to the fact that compared to aluminum alloys, ferrous alloys typically exhibit significantly lower thermal diffusivity. Consequently, FSW of steels tends to encounter more severe conditions when it comes to the choice of welding tools[3]. The utilization of FSW in the context of aluminum alloys was initially driven by the challenge of weldability. Traditional fusion welding methods often struggled to produce defect-free welds in aluminum alloys [4]. At present, there is a growing need to apply FSW in steels in consideration of economic cost, efficiency, and safety reasons. Furthermore, the integration of AI and robotic technology has expanded the possibilities for FSW in steel, making underwater weld fabrication and maintenance feasible.

This thesis aims to capture the elastic material properties of each material zone in FS welded joints. To accurately describe the elastic properties of a certain material several parameters such as Young's modulus and Poisson's ratio are necessary. Conventionally destructive testing techniques like global tensile test until failure will be carried out to obtain these property values. For uniform material, this methodology turns out to be efficient and useful. After which some measuring methods like strain gauges will be applied to obtain the strain field of the material.

However, for FSW joints, which consist of multiple material zones the methodology needs to be updated. During the tensile testing of FSW joints, failures often occur in the base material, leading to a lack of complete information about the actual static mechanical properties of the welded joints. A useful technique is local testing such as hardness tests in each material zone. In addition, a non-destructive technique like Digital Image Correlation (DIC) can be adopted. DIC offers an advantage over strain gauges in that it provides full-field measurement in each direction so that it allows the establishment of local values in each material zone when inhomogeneous properties are expected. In order to obtain accurate estimates dedicated displacement fields and material region allocations are required. In this thesis, DIC will be adopted as the main technique for obtaining the displacement and strain field, and for the allocation of the material region, the preliminary idea was to compare and optimize the sum of the squared difference of the displacement field between DIC and FEM test results to obtain the most likely material region boundaries.

1.2. Research Objectives

Following the Research Questions raised in the literature study (Chapter 2), the objectives of this thesis work can be represented by one research question with three sub-questions.

RESEARCH QUESTION

How to capture the elastic static strength properties of friction stir welded joint material zones, in relation to the welding parameters?

Which can be divided into several sub-questions according to the experiment procedure:

- **Sub-question 1**: Which DIC formulation is best suited to capture accurate and robust displacement and strain field description at the acceptable computational test?
- **Sub-question 2**: How to capture the elastic mechanical properties using Digital Image Correlation?
- **Sub-question 3**: How to partition the FSW joint material zones in order to capture the elastic mechanical properties for each one of them?

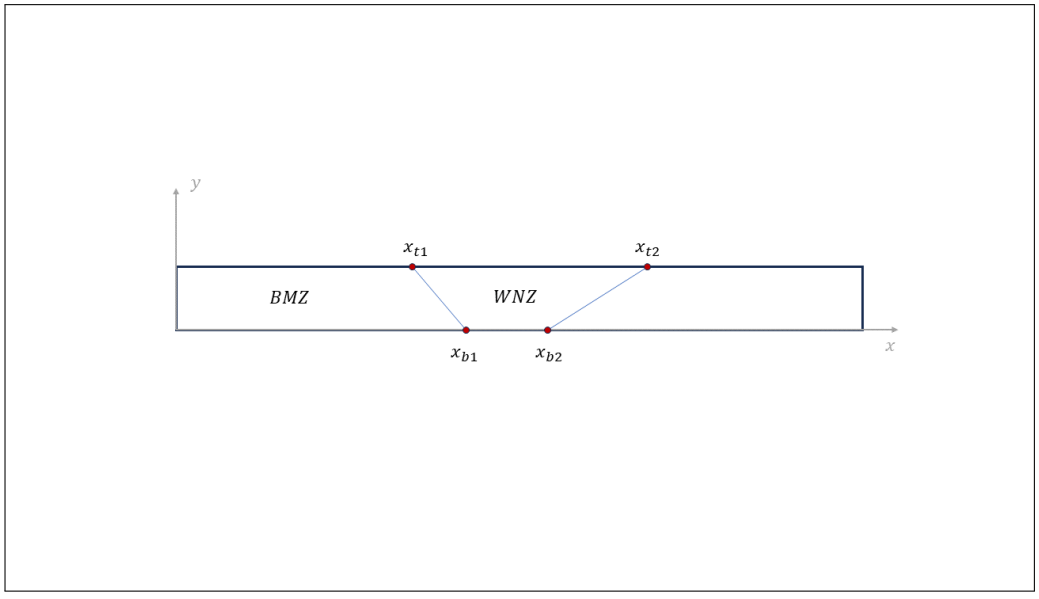

Figure 1.2: By optimizing the value of $x_{t1}, x_{t2}, x_{b1}, x_{b2}$ the boundary of different material areas can be determined

1.3. Report Outline

This report consists of 6 chapters: Introduction of the thesis work (chapter 1); Literature Review for the theoretical background of the applied methodology, including fundamentals of solid mechanics and digital image correlation method (chapter 2); Design of the tensile test and FEM simulation(chapter 3); Preliminary analysis on the DIC images for the verification of following work (chapter 4); Result of DIC and FEM analysis (chapter 5); Discussion for the results and concluding remarks (chapter 6).

2

Literature Review

2.1. Elastic Material Properties

Young's Modulus

Young's modulus is the modulus elasticity in tension or compression. In the elastic regime, it is calculated by dividing the tensile stress by the axial strain.

$$E = \frac{Tensile\ stress}{Axial\ strain} = \frac{\sigma}{\varepsilon} \tag{2.1}$$

In a plastic regime, where permanent deformation happens, Young's modulus would decrease accordingly. This can be explained by the dislocations and rearrangements of the material's atomic structure, which would result in an increased number of defects and reduced stiffness.

Different types of steel may exhibit slightly different responses in terms of Young's modulus during the plastic regime, it can be better described by the stress-strain curve. The mechanical behaviors in plastic regimes are not covered in this thesis, however.

Poisson's ratio

Poisson's ratio is the ratio of the amount of lateral contraction to the amount of axial elongation that occurs when a material is stretched or compressed in one direction.

$$\nu = -\frac{\varepsilon_{lateral}}{\varepsilon_{axial}} \tag{2.2}$$

Shear Modulus

Shear modulus is the ratio of shear stress to shear strain in the elastic range of deformation for a material. It can be formulated with a relation between Young's modulus and Poisson's ratio:

$$G = \frac{E}{2(1+\nu)} \tag{2.3}$$

Yield Point

According to the definition of ASTM international[5], yield point refers to the stress at which an increase in strain occurs without an increase in stress. In stress-strain curve, it is typically characterized by a sharp knee or discontinuity.

Yield Strength

Yield strength is the stress at which a material exhibits a specified limiting deviation from the proportionality of stress to strain. A commonly used determination method for yield strength is 0.2% **Offset Method**, where a line with the specified offset parallel to the stress-strain curve is plotted to determine the strength value.

Another useful method for determining the yield strength is **Extension Under Load Method**. It is for material whose stress-strain characteristics are well known from previous tests of similar material in which stress-strain diagrams was plotted, the total strain corresponding to the stress at which the specified offset (typically chosen as 0.5% by ASTM[5]) occurs will be known within satisfactory limits. The stress on the specimen, when this total strain is reached, is the value of the yield strength.

In this case, due to the fact that the stress-strain characteristics are unknown for the specimen **Offset Method** is preferred to be applied if applicable.

Ultimate Tensile Strength
Ultimate tensile strength (Ultimate Tensile Strength (UTS)) is the maximum stress that a material can withstand before fracture or failure in tension test, it is the highest stress value observed on the stress-strain curve. The calculation of UTS can be done by dividing the maximum load the specimen sustains during a tension test by the original cross-sectional area of the specimen.

Elongation
Elongation at fracture is defined as the elongation measured prior to the sudden decrease in force. For some ductile materials that may not exhibit a sudden decrease in force, elongation can be taken as the strain measured prior to when the force falls below 10% of the maximum force encountered during the test.

2.2. 2D Digital Image Correlation Principle

Digital Image Correlation is a non-contact optical technique used to measure displacement and strain field on the surface of structures. With more than 2 cameras 3-D DIC can also be adopted to measure out-of-plane displacements.
A typical DIC procedure contains the following steps:

1. Preparation of the analyzed specimen surface: The difficulty for the computer to identify the correspondence of a single pixel between two images is often referred to as an aperture problem, or more generally, correspondence problem. A conventional solution is to spray a unique pattern of random speckles/dots on the specimen surface. To resolve the correspondence problem, i.e. to establish a unique correspondence of certain pixels between images, an idealized surface texture shall be isotropic and non-periodic.

2. Calibration of the device: Before image recording, the calibration of the device especially for the camera is required, to make sure the relative position of the observed image is recorded accurately in the specified coordinate system.

3. Reference and deformed Image recording: Once the device along with the specimen is well prepared, the experiment can be carried out during which the camera should take a group of pictures to record the deforming process of regions of interest (Region Of Interest (ROI)). Usually, high-speed cameras are needed for a complete recording process. For measuring static mechanical characteristics, the images are often taken when the load has been applied, thus the load is typically set up in a trapezoidal way where the deformed images will be taken when the applied load remains constant.
   For 2-dimensional problems, a single camera that is normal to the specimen surface shall be installed while for 3-dimensional problems two cameras from different directions are necessary for recording out-of-plane deformation and strain.

4. Image analysis with specialized algorithm: As mentioned above, for computers the deformation and strain information should be described in mathematical terms so that the following calculation can be done. Conventionally the analysis will be carried out as an optimization problem, where all the pixels in ROI are scanned through to find the best correspondence. Typical calculation method includes Normalised Cross-correlation (Normalised Cross-Correlation (NCC)) which aims at finding the maximum of the local subset and Least-Square Matching (Least-Square Matching (LSM)) which calculated the Sum of Squared Differences (Sum of Squared Differences (SSD)) to find the minimum. Based on the subset region to be calculated in each step, DIC algorithms can be categorized as local DIC method and global DIC method, the discussion of which will be covered in the sections below.

5. Visualization of result: The last step of the DIC technique is visualization, where the displacement or strain field is usually plotted as a contour plot to visualize the experiment result. The filtered result along with the typical error distribution can also be illustrated via visualization.

2.2.1. 2-D measurements

Camera Calibration

Camera calibration includes the process of relating several coordinate systems. The most widely used camera model is the Pinhole Camera Model, which relates the location of a certain point in the world coordinate system (denoted as $\hat{\underline{\mathbf{x}}}_w = [\hat{x}_w \ \hat{y}_w \ \hat{z}_w \ 1]^T$) to the idealized location in the image sensor coordinate system (denoted as $\hat{\underline{\mathbf{x}}}_s = [\hat{x}_s \ \hat{y}_s \ 1]^T$). The circumflex means undistorted[6]. The pinhole camera model principle can be expressed as:

$$\alpha\hat{\underline{\mathbf{x}}}_s = \mathbf{KV}\hat{\underline{\mathbf{x}}}_w \tag{2.4}$$

Where **K** is the intrinsic camera parameter matrix:

$$\mathbf{V} = \begin{bmatrix} \xi_x & c_s & c_x \\ 0 & \xi_y & c_y \\ 0 & 0 & 1 \end{bmatrix} \tag{2.5}$$

Here ξ_x and ξ_y scales the units from metric units to units of pixels. c_s and c_y apply the translation such that the origin of the sensor coordinate system is located at the top left of the image. c_s performs converts an orthogonal coordinate system into a screwed sensor coordinate system. In the case of an orthogonal sensor coordinate system, $c_s = 1$.

And **V** is the extrinsic camera parameter matrix:

$$\mathbf{K} = \begin{bmatrix} R_{11} & R_{12} & R_{13} & T_1 \\ R_{21} & R_{22} & R_{23} & T_2 \\ R_{31} & R_{32} & R_{33} & T_3 \end{bmatrix} \tag{2.6}$$

which contains the rotation matrix **R** and translation vector **T**.

Apart from the pinhole camera model, a radial distortion model is also necessary for converting the ideal sensor coordinate system to the actual image sensor coordinate system, which is distorted (denoted as $\underline{\mathbf{x}}_n = [x_n \ y_n]^T$). Firstly, the homogeneous coordinates in the sensor coordinate system need to be normalized(denoted as $\hat{\underline{\mathbf{x}}}_n = [\hat{x}_n \ \hat{y}_n]^T$):

$$\hat{\underline{\mathbf{x}}}_n = \begin{bmatrix} 1 & 0 & 0 \\ 0 & 1 & 0 \end{bmatrix} \left(\mathbf{K}^{-1}\hat{\underline{\mathbf{x}}}_s\right) \tag{2.7}$$

In addition, the relation between idealized and actual image coordinates has to be established:

$$\mathbf{x}_n = (1 + \kappa_1 \hat{\underline{\mathbf{x}}}_n^T \hat{\mathbf{x}}_n + \kappa_s (\hat{\underline{\mathbf{x}}}_n^T \hat{\mathbf{x}}_n)^2)\hat{\mathbf{x}}_n \tag{2.8}$$

2.3. Texture Quality Analysis

A successful DIC analysis is ensured by a qualified image texture. Hence some priori analysis needs to be done to evaluate the images to be analyzed afterward, a significant characteristic of the texture is the grayscale histogram, which illustrates the grayscale distribution within the ROI, a typical histogram of the specimen along with the specified ROI is as shown in Figure 2.1 and 2.2 below.

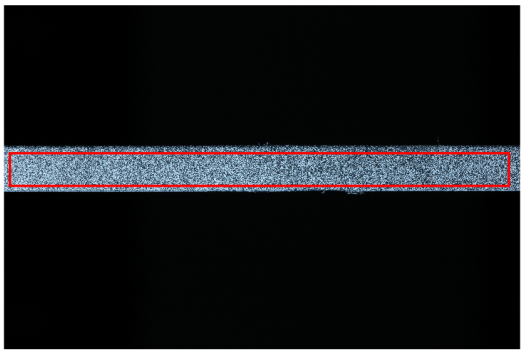

Figure 2.1: ROI of the sample cross-section

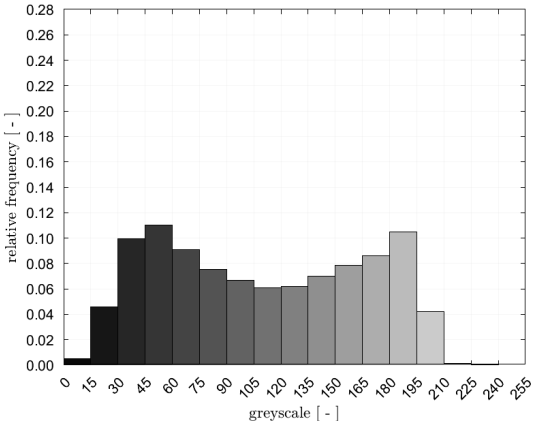

Figure 2.2: Gray scale level histogram within the ROI

There are several aspects requiring particular attention. First is the effective range, which indicates the similarity of the black and white texture. The wider the effective range, the better the uniqueness. In this example, the grayscale ranges from 0 to 210, which is qualified enough for further investigation. Besides, there is no pure reflection(grayscale = 255) appearing in this case and saturation(grayscale = 0) is also limited, which indicates a nice texture quality.

Another property to be emphasized is the saturation problem, which is the white color(255) ratio of the histogram. The saturation ratio should be as small as possible to prevent reflection, in this case merely no distribution can be observed within the range of 240-255, thus the effectiveness of the texture can be guaranteed.

To further evaluate the texture quality some quantified criteria will be applied. Hild and Roux[7] [8] has provided some useful criteria to carry out the evaluation. For the fluctuation properties the subset gray level standard deviation (Standard Deviation (SD)) can be calculated. Practically a limit is set as at least 1% of the dynamic range of the camera, to ensure that there are enough gradients for the camera to capture the displacements. A typical result of the sample specimen is shown in Figure 2.3 and 2.4 below.

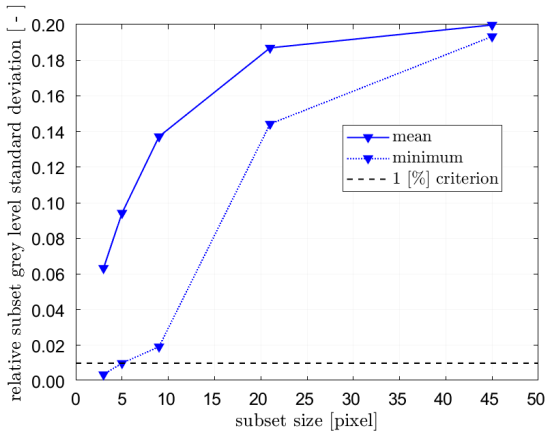

Figure 2.3: Gray scale SD for different subset sizes

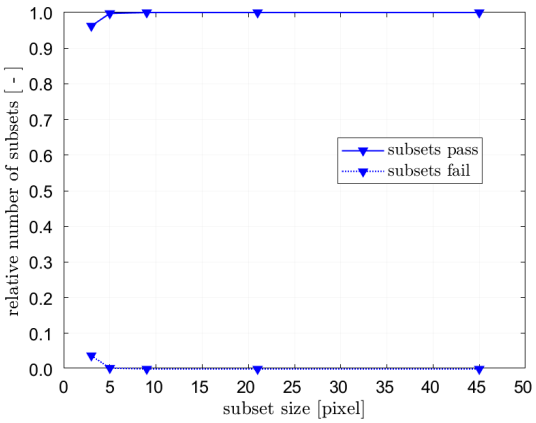

Figure 2.4: Subset grayscale level percentage pass

As depicted in the figures above, for a subset size bigger than 5 pixels the criterion can be satisfied.

Another useful principle is correlation radii, which different from SD, shall be normalized by the element size first. This parameter can be computed from the parabolic interpolation of the auto-correlation function. The two correlation radii ξ_1, ξ_2, calculated from the inverse of the curvature eigenvalues, shall be as close as

enough(isotropic) and as small as possible(unique). The limitation is chosen to be 25% of the element size. An example is shown in Figure 2.5 and 2.6 below.

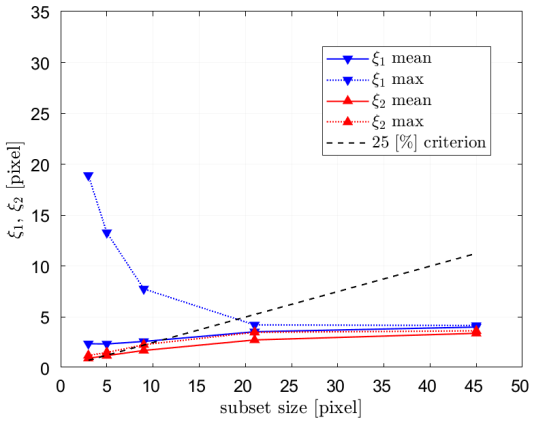

Figure 2.5: Mean and max correlation radii

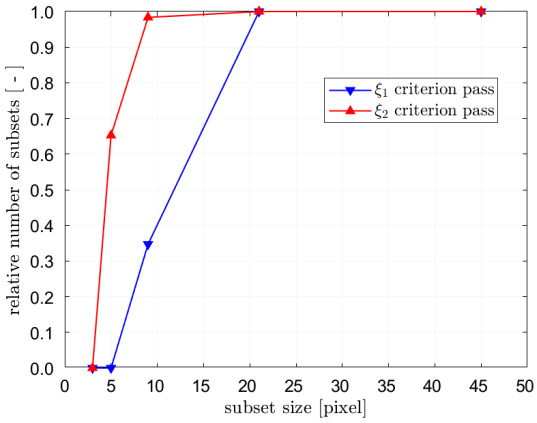

Figure 2.6: Correlation radii percentage pass

In this case, it can be observed that for a subset size bigger than 21 pixels, the criterion can be perfectly met.

2.4. Kinematic basis functions

The displacement field refers to the vector field that describes the displacement of points in the material as a function of their spatial coordinates. The strain field, on the other hand, is defined as the tensor field that describes the change in shape or size of an infinitesimal element of the material as a function of its position within the material.

The basic principle of DIC is tracking the displacement of small subsets within ROI. Kinematic basis functions are mathematical functions used to describe the deformation of the subsets. Due to the fact that subsets are pre-discretized, it is necessary to interpolate the displacements measured at discrete pixel locations within the ROI to estimate the continuous deformation field.

There are several types of kinematic basis functions in DIC, including polynomial functions, B-splines and some other special formulations. The choice of basis functions depends on the specific requirements on desired accuracy and computational efficiency.

B-Splines

In the measurement of displacement and strain field, some unwanted variations or errors, which are often referred to as noise, would appear. The presence of noise in the measurement of the displacement field can lead to inaccuracies and errors in the measured data, which can affect the reliability and validity of the results obtained. To obtain an accurate strain field polynomial filters like Savitzky-Golay smoothing and differentiation filter or Airy stress function can be adopted.

Cheng et al.[9] used the B-Spline function to represent the object deformation field throughout the entire image area, optimizing the control variables within the B-Spline deformation function iteratively with the Levenberg-Marquardt method to achieve minimum disparity between the predicted and actual deformed images.

B-spline formulation is a mathematical technique to represent and interpolate complex curves or surfaces using piecewise polynomial functions. The two-dimensional deformation function for the regions of interest can be written in parametric form:

$$D(\alpha,\beta) = \{u(\alpha,\beta), v(\alpha,\beta)\}^T \tag{2.9}$$

where (α, β) are parameter coordinates and $0 \leq \alpha, \beta \leq 1$. By varying coefficients in the deformation function, a full-field optimal match of the intensity patterns can be obtained, resulting in a full-field description of the deformations throughout the regions of interest.

Savitzky-Golay filter
Savitzky-Golay filter is a type of digital filter widely used in engineering for smoothing and differentiation of noisy signals. The key idea is to have a polynomial fit for the given data points at a specified window size and estimate the smoothed value at the middle point of the window[10].

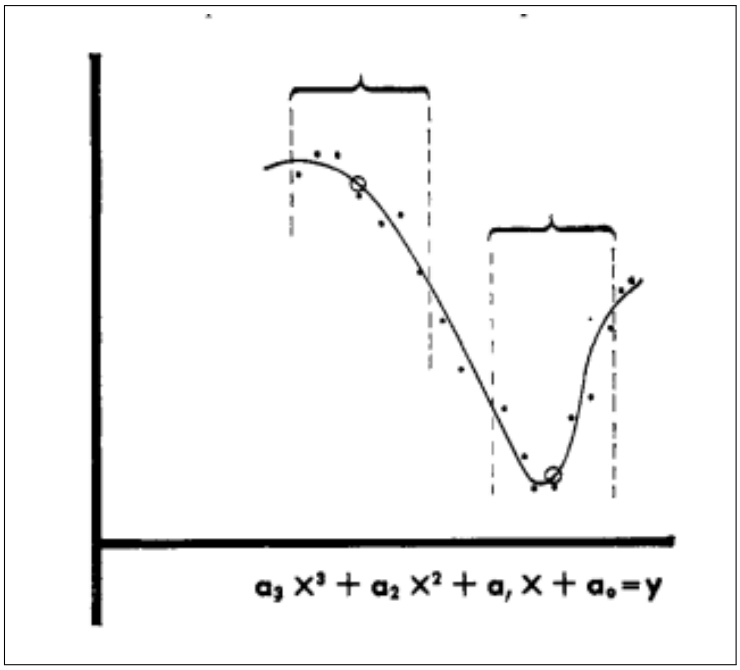

Figure 2.7: An example of a 3rd-order Savitzky-Golay filter with a window size of 7 points

2.5. Local (subset-based) formulation

The basic principle of DIC is to estimate 2D or 3D displacements and displacement derivatives by matching the image textures before and after deformation[11]:

$$g(\mathbf{X}) = f(\mathbf{X} + \mathbf{u}(\mathbf{X})) \tag{2.10}$$

where $\mathbf{u}(\mathbf{x})$ denotes 2D or 3D displacements and $f(\mathbf{X})$ and $g(\mathbf{X})$ denotes the image texture distribution before and after deformation respectively. The equation itself represents the conservation of optical flow.

Based on the definition above, the mapping problem can be transformed into an optimization problem[12][13], which can be expressed by the SSD correlation function:

$$\min_{y(\mathbf{X})} \int_{\Omega} |f(\mathbf{X}) - g(y(\mathbf{X}))|^2 d\mathbf{X} \tag{2.11}$$

or Cross-correlation function:

$$\max_{y(\mathbf{X})} \int_{\Omega} f(\mathbf{X}) g(y(\mathbf{X})) d\mathbf{X} \tag{2.12}$$

Local DIC algorithm, often referred to as local subset DIC method, is commonly adopted by many commercial DIC software [14]. The main idea is to divide the regions of interest into a finite number of local subsets $\Omega = \bigcup \Omega_i$ and calculate the optimization problem for each subset in parallel. The deformation of which is assumed to be piecewise affine as:

$$y(\mathbf{X}) = \mathbf{X} + \sum_i (u_i + \mathbf{F}_i(\mathbf{X} - \mathbf{X}_{i0}))\chi_i(\mathbf{X}) \tag{2.13}$$

Where u_i and $\mathbf{F}_i$ are constant, denoting displacement and displacement gradient for each Ω_i. χ_i is the index function to include only the deformation within the chosen subset.

$$\chi_i = \begin{cases} 1, \mathbf{X} \in \Omega_i \\ 0, \mathbf{X} \notin \Omega_i \end{cases} \tag{2.14}$$

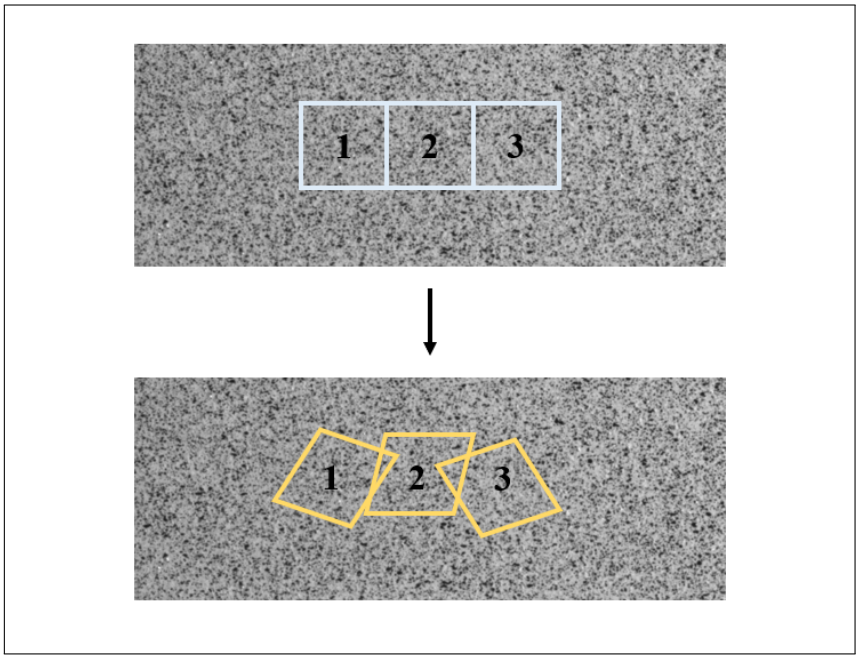

Figure 2.8: Illustration of Local DIC method

As a result, the formulation of the optimization problem in the local DIC method goes:

$$\underset{\mathbf{F}_i, \mathbf{u}_i}{min} = \int_{\Omega_i} |f(\mathbf{X}) - g(\mathbf{X} + \sum_i (u_i + \mathbf{F}_i(\mathbf{X} - \mathbf{X}_{i0}))\chi_i(\mathbf{X}))|^2 d\mathbf{X} \tag{2.15}$$

Due to the fact that in the local subset DIC method, different subsets are solved in parallel, it has the advantage of fast computation and convergence speed. However, the solved displacement field might be incompatible because of the independent calculation for each subset. In addition, the subset size in the local DIC method can not be too small or too large.

ADIC2D framework

Atkinson and Becker[15] has developed a so-called ADIC2D framework which is a 2-dimensional subset-based(local) DIC method consistent with state-of-the-art techniques.

As illustrated above, the DIC procedure contains 4 processes: calibration, correlation, displacement, and strain computation. For calibration, ADIC2D uses a pinhole camera model as in 2.2.1. For correlation, ADIC2D adopts the criterion of ZNCC the same as in the RG-DIC algorithm.

In the DIC technique to describe the deformed shape of a certain subset different orders of shape functions(SF) are required. The most frequently used SFs are zero, first and second-order ones:

$$\mathbf{W}^{SF0}(\Delta x_i, \mathbf{P}^{SF0}) = \begin{bmatrix} 1 & 0 & u \\ 0 & 1 & v \end{bmatrix} \begin{bmatrix} \Delta x_i \\ \Delta y_i \\ 1 \end{bmatrix} \tag{2.16}$$

$$\mathbf{W}^{SF1}(\Delta x_i, \mathbf{P}^{SF1}) = \begin{bmatrix} 1+u_x & u_y & u \\ v_x & 1+v_y & v \end{bmatrix} \begin{bmatrix} \Delta x_i \\ \Delta y_i \\ 1 \end{bmatrix} \tag{2.17}$$

$$\mathbf{W}^{SF2}(\Delta x_i, \mathbf{P}^{SF2}) = \begin{bmatrix} \frac{1}{2}u_{xx} & u_{xy} & \frac{1}{2}u_{yy} & 1+u_x & u_y & u \\ \frac{1}{2}u_{xx} & u_{xy} & \frac{1}{2}u_{yy} & v_x & 1+v_y & v \end{bmatrix} \begin{bmatrix} \Delta x_i^2 \\ \Delta x_i \Delta y_i \\ \Delta y_i^2 \\ \Delta x_i \\ \Delta y_i \\ 1 \end{bmatrix} \tag{2.18}$$

Where u and v represent the displacement in x- and y-directions respectively and the subscripts denote their first and second-order derivatives. P, which is a vector contains all the different elements in the coefficient matrix, can be expressed as:

$$\begin{aligned} \mathbf{P}^{SF0} &= [u\,v]^T \\ \mathbf{P}^{SF1} &= [u\,u_x\,u_y\,v\,v_x\,v_y]^T \\ \mathbf{P}^{SF2} &= [u\,u_x\,u_y\,u_{xx}\,u_{xy}\,u_{yy}\,v\,v_x\,v_y\,v_{xx}\,v_{xy}\,v_{xy}]^T \end{aligned} \tag{2.19}$$

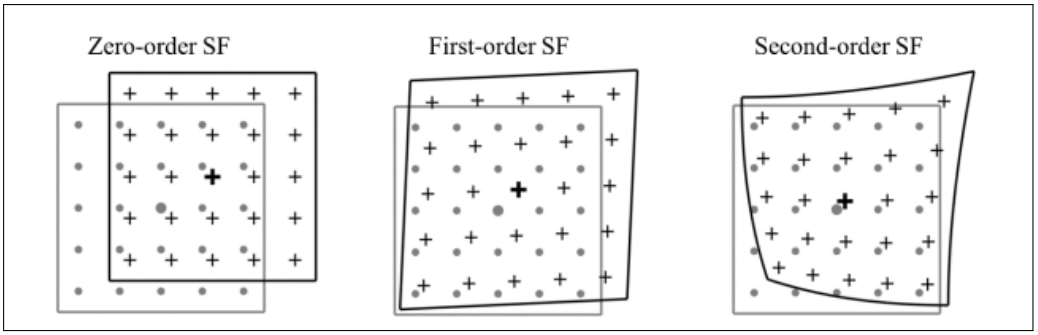

Figure 2.9: Deformation of subsets for different SF orders[6]

2.6. Global (finite element based) formulation

In contrast to the local DIC method, the global DIC method solves the deformation of the chosen ROI still in a whole. It usually is based on finite element discretization, thus often referred to as Finite Element Global DIC as well. Due to this, the compatibility between subsets is guaranteed:

$$\mathbf{y}(\mathbf{X}) = \mathbf{X} + \mathbf{u}(\mathbf{X}) = \mathbf{X} + \sum_p u_p \psi_p(\mathbf{X}) \tag{2.20}$$

Where $\psi_p(\mathbf{X})$ are global basis functions and u_p are the degrees of freedom to be solved. After substitution into equation 2.11, the problem becomes minimization over u_p, which can be further simplified by Taylor expansion, using first-order approximation as:

$$\mathbf{u}_{k+1} = \mathbf{u}_k + \delta\mathbf{u} \tag{2.21}$$

$$g(\mathbf{y}(\mathbf{X})) = g(\mathbf{X} + \mathbf{u}_k(\mathbf{X}) + \delta\mathbf{u}) \approx g(\mathbf{X} + \mathbf{u}_k(\mathbf{X})) + \nabla g \cdot \delta\mathbf{u}(\mathbf{X}) \tag{2.22}$$

In that way, the optimization problem becomes:

$$\underset{\mathbf{u}_p}{min} = \int_\Omega |f(\mathbf{X}) - g(\mathbf{X} + \mathbf{u}_k(\mathbf{X}) - (\sum_p \delta u_p \psi_p(\mathbf{X})) \cdot \nabla g(\mathbf{X})|^2 \tag{2.23}$$

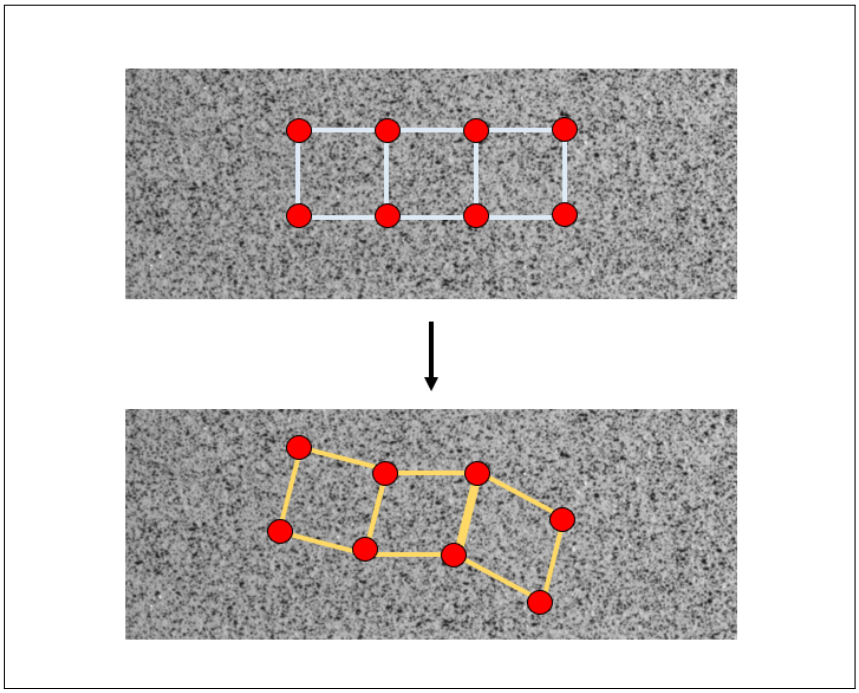

Figure 2.10: Illustration of Global DIC method

The Global DIC method deals with the computational effort in series while not in parallel, which leads to a more expensive computational cost. However, as mentioned above, kinematic compatibility or continuity is guaranteed in the Global method, which brings the improvement of accuracy, being the leading advantage of the Global DIC method.

Airy stress
In FEM analysis to reduce the computational cost of analyzing large structural systems usually super element formulation would be employed, among which airy stress function is the most conventional method.

The Airy stress function is commonly used to analyze the stress and strain field in two-dimensional elastic solids. It is defined as a scalar function of the coordinates x and y, which satisfies the bi-harmonic equation. The bi-harmonic equation is a fourth-order partial differential equation describing the equilibrium of the stresses in a two-dimensional elastic solid which can be solved by appropriate boundary conditions. The Airy stress function is particularly useful for problems involving circular or axisymmetric geometries. A typical Airy Stress function which only takes into account the stress components in axial (y) direction is[11]:

$$\varphi = C_{22}y^2 + C_{33}y^3 \tag{2.24}$$

In Cartesian coordinates the stress components are defined as:

$$\begin{aligned} \sigma_{xx} &= \frac{\partial^2 \varphi}{\partial y^2} = 2C_{22} + 6C_{33}y \\ \sigma_{yy} &= \frac{\partial^2 \varphi}{\partial x^2} = 0 \\ \sigma_{xy} &= -\frac{\partial^2 \varphi}{\partial x \partial y} = 0 \end{aligned} \tag{2.25}$$

Considering that in 2D-DIC measurement the strain is measured on the surface, a plane stress condition can

be assumed to introduce Hooke's law:

$$\begin{aligned}\varepsilon_{xx} &= \frac{(\kappa+1)\sigma_{xx}-(3-\kappa)\sigma_{yy}}{8G} = \frac{(\kappa+1)(6C_{33}y+2C_{22})}{8G}\\ \varepsilon_{yy} &= \frac{(\kappa+1)\sigma_{yy}-(3-\kappa)\sigma_{xx}}{8G} = -\frac{(3-\kappa)(6C_{33}y+2C_{22})}{8G}\\ \varepsilon_{xy} &= \frac{\sigma_{xy}}{2G} = 0\end{aligned} \tag{2.26}$$

with Kolosov's constant:

$$\kappa = \frac{3-\nu}{1+\nu} \tag{2.27}$$

and small strain-displacement relations:

$$\begin{aligned}\varepsilon_{xx} &= \frac{\partial u_x}{\partial x}\\ \varepsilon_{yy} &= \frac{\partial u_y}{\partial y}\\ \varepsilon_{xy} &= \frac{1}{2}(\frac{\partial u_y}{\partial x}+\frac{\partial u_x}{\partial y})\end{aligned} \tag{2.28}$$

In complex coordinates, the displacement field can be obtained including the rigid body terms by:

$$\begin{aligned}\mathbf{u}(z) &= u_x + i\,u_y\\ &= \sum_k C_k \mathbf{\Psi}_k\\ &= C_x + C_y\cdot i + C_r\cdot(ix-y)+\\ &(\frac{C_{22}}{G})\cdot\frac{2(\kappa+1)x-2(3-\kappa)iy}{8}+\\ &(\frac{C_{33}}{G})\cdot\frac{-3(\kappa+1)ix^2+6(\kappa+1)xy-3(3-\kappa)iy^2}{8}\end{aligned} \tag{2.29}$$

In Commercial software (Istra4D, Dantec Dynamics) the amplitudes C_k can be obtained by solving the equation $[\mathbf{\Psi}]C = \mathbf{u}(z)_{Istra4D}$. Due to the fact that $[\mathbf{\Psi}]$ is non-square and rank-deficient, the solution can by calculated by minimizing $||[\mathbf{\Psi}]C - \mathbf{u}(z)_{Istra4D}||^2$ over C_k.

2.7. Hybrid formulation

Augmented Lagrangian DIC Method

Based on Wang and Pan's work of comparison study between the subset-based local DIC method and FE-based global DIC method[16], local DIC provides with theoretically smallest normalized standard deviation errors (Standard Deviation Errors (SDE)), but the differences between the methods turns out to be minor in numerical experiments. As for computation cost, local DIC also gives rise to the fastest calculation speed and least average iteration number(Average Iteration Number (AIN)). In addition, with the recently developed Inverse Compositional Gauss-Newton(Inverse Compositional Gauss-Newton method (IC-GN)) algorithm combined with reliability-guided displacement tracking (Reliability-Guided Displacement Tracking (RGDT)) strategy[17], the efficiency of the Local DIC method can be further improved. Although appearing superior to the Global DIC method in both aspects, it should be noted that global Q8-DIC(8-node FE-based DIC) has a potential advantage over the Local DIC method with regard to robustness when dealing with heterogeneous deformation problems.

To combine the advantages of local and global DIC methods, an augmented Lagrangian DIC (Augmented Lagrangian DIC (ALDIC)) was promoted by Yang and Bhattacharya. ALDIC takes the global constraint which was neglected by the Local method and adopted by the Global method into account:

$$\{\mathbf{F}\} = \mathbf{D}\,\{\mathbf{u}\} \tag{2.30}$$

Where **D** denotes the discrete gradient operator, in this case, first-order finite difference based on a uniform square mesh is adopted that:

$$\mathbf{D} = \frac{1}{2h}\begin{bmatrix} -2 & 2 & & & & \\ -1 & 0 & 1 & & & \\ & -1 & 0 & 1 & & \\ & & \ddots & \ddots & \ddots & \\ & & & -1 & 0 & 1 \\ & & & & -2 & 2 \end{bmatrix} \tag{2.31}$$

Here h is the distance between nodes.
Lagrange multiplier which enforces the constraint was introduced to the ansatz 2.13 and the optimization problem becomes:

$$\begin{aligned} \underset{\mathbf{F}_i,\mathbf{u}_i,\hat{\mathbf{u}}_i}{min} = &\int_{\Omega_i} (|f(\mathbf{X}) - g(\mathbf{X} + \sum_i (u_i + \mathbf{F}_i(\mathbf{X} - \mathbf{X}_{i0})))|^2 \\ &+ \frac{\beta}{2}|(\mathbf{D}\hat{\mathbf{u}})_i - \mathbf{F}_i|^2 + \nu_i : ((\mathbf{D}\hat{\mathbf{u}})_i - \mathbf{F}_i) + \frac{\mu}{2}|\hat{\mathbf{u}}_i - \mathbf{u}_i|^2 + \lambda_i \cdot ((\hat{\mathbf{u}})_i - \mathbf{u}_i))d\mathbf{X} \end{aligned} \tag{2.32}$$

By setting $\mathbf{W}_i := \frac{\nu}{\beta}, \mathbf{v}_i := \frac{\lambda_i}{\mu}$, the problem can be defined as:

$$\begin{aligned} \underset{\mathbf{F}_i,\mathbf{u}_i,\hat{\mathbf{u}}_i,\mathbf{W}_i,\mathbf{v}_i}{min} = &\int_{\Omega_i} (|f(\mathbf{X}) - g(\mathbf{X} + \sum_i (u_i + \mathbf{F}_i(\mathbf{X} - \mathbf{X}_{i0})))|^2 \\ &+ \frac{\beta}{2}|(\mathbf{D}\hat{\mathbf{u}})_i - \mathbf{F}_i + \mathbf{W}_i|^2 + \frac{\mu}{2}|\hat{\mathbf{u}}_i - \mathbf{u}_i + \mathbf{v}_i|^2)d\mathbf{X} \end{aligned} \tag{2.33}$$

In this way, the optimization problem appears in the form of minimizing quadratic terms over $\{\mathbf{F}_i\}, \{\mathbf{u}_i\}, \{\hat{\mathbf{u}}_i\}$ and Lagrange multipliers $\{\mathbf{W}_i\}, \{\mathbf{v}_i\}$.
To solve it, an alternating direction method of multipliers (Alternating Direciton Method of Multipliers (ADMM)) is adopted where the global problem is divided into 3 local subproblems. The task is to find out the $(k+1)$th update with given $\{\mathbf{F}_i^k\}, \{\mathbf{u}_i^k\}, \{\hat{\mathbf{u}}_i^k\}, \{\mathbf{W}_i^k\}, \{\mathbf{v}_i^k\}$:

1. Local update. Holding $\{\hat{\mathbf{u}}_i^k\}, \{\mathbf{W}_i^k\}, \{\mathbf{v}_i^k\}$ fixed to find the optimized $\{\mathbf{F}_i^{k+1}\}, \{\mathbf{u}_i^{k+1}\}$

2. Global update. Holding $\{\mathbf{F}_i^{k+1}\}, \{\mathbf{u}_i^{k+1}\}, \{\mathbf{W}_i^k\}, \{\mathbf{v}_i^k\}$ fixed to find the optimized $\{\hat{\mathbf{u}}_i^{k+1}\}$.

3. Lagrange multiplier update. Holding $\{\mathbf{F}_i^{k+1}\}, \{\mathbf{u}_i^{k+1}\}, \{\hat{\mathbf{u}}_i^{k+1}\}$ to find the optimized $\{\mathbf{W}_i^{k+1}\}, \{\mathbf{v}_i^{k+1}\}$.

It shall be noted that practically the displacement is the most important point. Hence, only $(\hat{\mathbf{u}}_{k+1} - \hat{\mathbf{u}}^k)$ being smaller than a tolerance value will be checked as the stopping criterion[12].

2.8. Reliability-guided formulation

In the conventional DIC method, for the purpose of saving computational cost, the computed displacements and strains of a specific point will be adopted as the initial guess of the next point. This path-dependent characteristic would give rise to errors in results, especially when there exists discontinuity in the structure and when the initial guess of the whole structure goes wrong. Simultaneously, if estimating the initial guess separately, the computational efficiency would decrease considerably.

To fix this disadvantage, Bing Pan[18] has proposed a reliability-guided digital image correlation(Reliability-Guided Digital Image Correlation (RG-DIC)) algorithm, which uses zero-mean normalized cross correlation (Zero-mean Normalized Cross Correlation (ZNCC)) coefficients to define the calculation path.

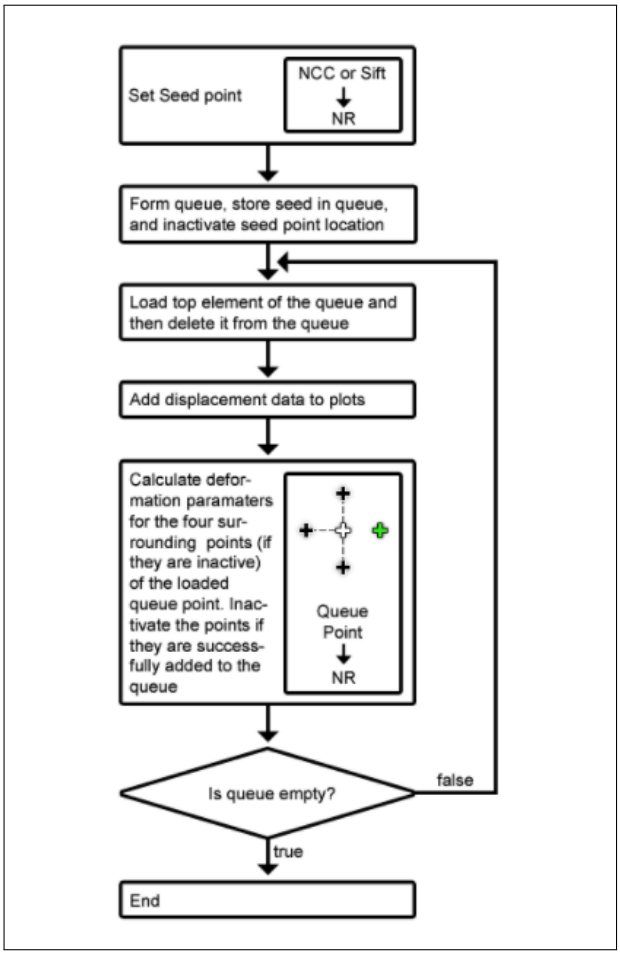

Figure 2.11: Flow chart of RG-DIC algorithm[18]

The zero-normalized sum of squared differences (Zero-Normalized Sum of Squared Differences (ZNSSD)) can be formulized as:

$$C_{ZNSSD}(\mathbf{p}) = \sum_{x=-M}^{M}\sum_{y=-M}^{M}\left[\frac{f(x,y)-f_m}{\sqrt{\sum_{x=-M}^{M}\sum_{y=-M}^{M}[f(x,y)-f_m]^2}} - \frac{g(x',y')-g_m}{\sqrt{\sum_{x=-M}^{M}\sum_{y=-M}^{M}[g(x',y')-g_m]^2}}\right]^2 \tag{2.34}$$

Like in conventional DIC methods, $f(x,y)$ denotes the reference image gray level intensity, and $g(x',y')$ denotes the deformed image gray level intensity. $\mathbf{p}$ is the desired vector according to the used displacement mapping function. And f_m, g_m denotes the mean intensity values of reference and deformed image respectively:

$$f_m = \frac{1}{(2M+1)^2}\sum_{x=-M}^{M}\sum_{y=-M}^{M}[f(x,y)] \tag{2.35}$$

$$g_m = \frac{1}{(2M+1)^2}\sum_{x=-M}^{M}\sum_{y=-M}^{M}[g(x',y')] \tag{2.36}$$

ZNCC can be related to ZNSSD via:

$$C_{ZNCC}(\mathbf{p}) = 1 - 0.5 \times C_{ZNSSD}(\mathbf{p}) \tag{2.37}$$

Assuming the subset center to be (x_0, y_0) and the distances of a certain point (x,y) from the center to be $\Delta x = x - x_0$ and $\Delta y = y - y_0$. The reference point and deformed point within the subset can be connected by the so-called "displacement mapping function"[19], which has its first-order linearized case as:

$$\begin{aligned} x' &= x_0 + \Delta x + u + u_x\Delta x + u_y\Delta y \\ y' &= y_0 + \Delta y + v + v_x\Delta x + v_y\Delta y \end{aligned} \tag{2.38}$$

Where u_x, u_y, v_x, v_y are the first-order displacement gradient components.

For the displacement component determination, the Newton-Raphson (Newton-Raphson method (NR)) method is adopted by the RG-DIC algorithm to find the iterative solution, which applies the first and second order of the Taylor series to approximately solve the equation based on the initial guess.

Different from other DIC methods, RG-DIC begins with the selection of a seed point, which needs special attention when there exists a crack in the structure for an additional requirement of continuity within the ROI. The illustration of seed point neighbor calculation is as depicted in Figure 2.12 below.

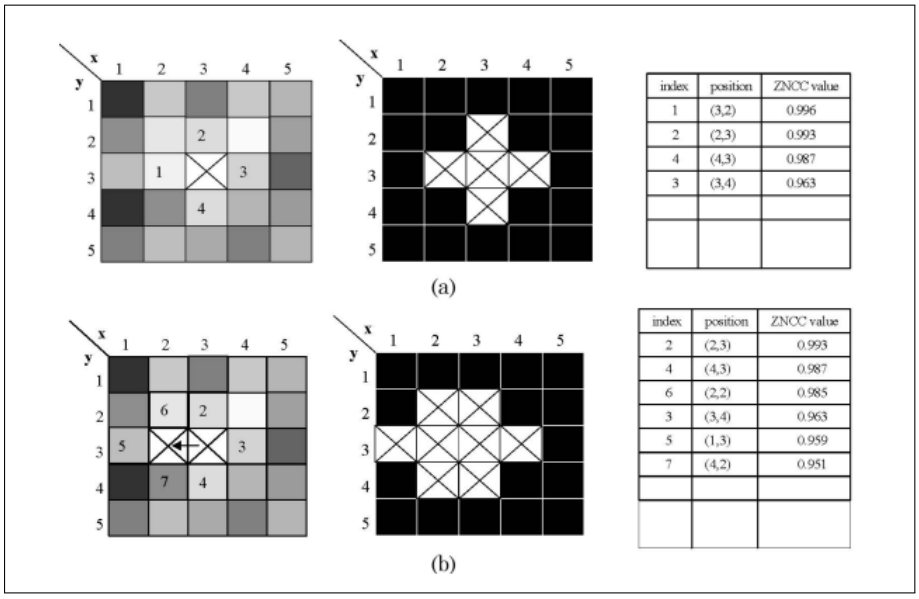

index	position	ZNCC value
1	(3,2)	0.996
2	(2,3)	0.993
4	(4,3)	0.987
3	(3,4)	0.963

index	position	ZNCC value
2	(2,3)	0.993
4	(4,3)	0.987
6	(2,2)	0.985
3	(3,4)	0.963
5	(1,3)	0.959
7	(4,2)	0.951

Figure 2.12: The neighbouring seed calculation procedure in RG-DIC method[20]

After the selection of the seed point, computation needs to be done for the ZNCC value of the 4 neighboring points of the seed point. The computation result will be put into a queue from higher to lower, where the highest one indicates the next seed point to be assigned. At any computation step, the top point with the highest ZNCC value is removed and the neighboring points of it are inserted into the queue in descending order. The computation steps are repeated until the queue is empty when all the points within ROI are covered.

In practical application, there are also validity checks and computation result checks by binary mask M_v and M_c to ensure continuity, for further explanation [18] shall be the reference paper. The flow chart of the RG-DIC algorithm is shown in Figure 2.11 below.

One potential problem of the RG-DIC method is that it is carried out serially. To resolve this, the open-source DIC software Ncorr chooses to process several seed points in parallel within the partitioned ROI[20].

2.9. Formulation performance

The above discussed the existing DIC methods, including the algorithm types and computation procedures. For the comparison study Bing et al.[16] have examined the performance of different DIC approaches based on both theoretical and experimental results. Their work has revealed the following conclusions:

1. The local(subset-based) DIC offers better precision than global(FEM-based) DIC methods. However, the improvement in accuracy is subtle enough to be neglected.

2. The local DIC exhibits higher efficiency than the global DIC. With the combination of a more robust and efficient IC-GN algorithm, the computational efficiency of local DIC methods is further improved.

Despite the proven superiority of local DIC methods, global DIC has several irreplaceable merits as follows:

1. Global DIC can directly establish the comparison between experimental results and numerical simulation results by the applied Finite Element meshes. It contributes to the minimization of the discretization error and conversely optimizes the numerical model in FEM analysis.
2. Global DIC can keep displacement robustness with smaller element size due to the global continuity constraints, which makes it more competent in case of greatly heterogeneous deformation.
3. Global DIC can guarantee the smoothness of the strain field.

Hild and Roux [**hild2012comparison**] have also made a comparison between local and global DIC approaches by using 4-noded zones of interest (local) and 4-noded elements (global). They have revealed that the global approach outperforms the local one thanks to the continuity requirements and the fact that shape functions span over four elements for inner nodes. Additionally, it was shown that more complex displacement fields can be captured by a global approach, and in the case of very noisy images, the displacement measurements would be more robust with a global approach.

Regarding the limitations of the different approaches a number of schemes have been proposed to address the potential problem. For the noiseness of the local DIC technique, Pan et al.[21] have advised to use Iterative Least Square algorithm (Iterative Least Square algorithm (ILS)) for displacement field and displacement gradient measurement and Pointwise Least Square algorithm (Pointwise Least Square algorithm (PLS)) for extracting the strain fields. The improvement in the efficiency and accuracy of the proposed scheme is verified through numerical simulation experiments. Zhao et al.[22] have proposed an Improved Hermite Finite Element Smoothing Method (Improved Hermite Finite Element Smoothing Method (IHFESM)) to extend the generality of the Hermite Finite Element Method by eliminating the contribution to the global regularization matrix from the invalid region. The effectiveness of which is verified. Avril et al.[23] have considered including diffuse approximation (Diffuse Approximation (DA)) into the local DIC technique, which has proven to be robust in application but more CPU time-consuming.

Algorithm	Computational Speed	Parallel Implementation	Displacement Compatibility	Strain Smoothness	Open Source
LOCAL					
Conventional	+	+	-	-	-
RG-DIC[18]	+	+	-	+	Yes
ADIC2D[15]	++	+	-	+	Yes
ILS-PLS[21]	+	+	-	+	No
IHFESM[22]	+	+	-	+	No
DA[23]	-	+	-	+	No
GLOBAL					
Conventional	-	-	+	+	-
ALDIC[12][13]	+	-	+	++	Yes
FEA[23]	+	-	+	+	No

Table 2.1: Comparison of different DIC algorithms

Table 2.1 gives an overview of the comparison between different DIC algorithms. The comparison is based on the paper's conclusions and is qualitative. For a quantitative comparison on this topic, further investigation is required, which will be covered in the final report. In the first stage of this thesis, the focus will be on applying the existing software to compute the mechanical properties, hence the algorithms with open-source codes will be adopted. In the last phase of the thesis, the emphasis will be on the improvement of the DIC method, thus the other or an innovative algorithm will be integrated into the existing framework.

2.10. Accuracy problems

2.10.1. Correlation error

During the DIC procedure, the occurring errors can be classified into statistical and systematical errors[24]. The statistical errors often occur because of the limited number of pixels and the corresponding gray values, if the uniqueness of the subset is not guaranteed (i.e. low texture quality as evaluated in chapter 2.3), the facet

position can't be determined accurately.
Systematical errors are usually resulting from the discretization of the real speckle pattern by the Charged-Coupled Device (CCD) pixels, and sometimes from the non-linear distortion of the facets. The latter source of errors can be minimized by Bundle Adjustment (BA) algorithm.
Statistical errors can be minimized by smoothing operations discussed in chapter 2.4 or by adding up new frames.

2.10.2. Out-of-plane displacement induced error

Sutton et al.[25] have studied the effects, especially the predicted strain errors due to out-of-plane translations and rotations in both 2D and 3D DIC techniques.

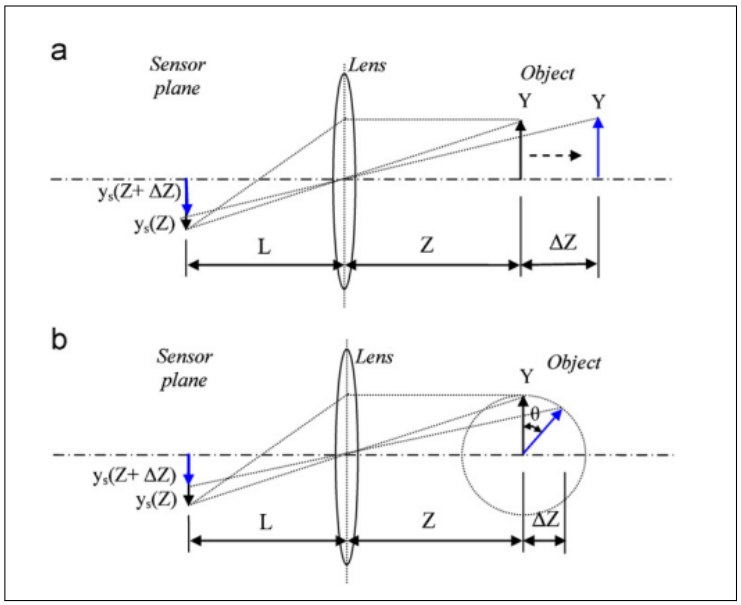

Figure 2.13: Effect of (a) out-of-plane translation and (b) rotation for a single-camera system[25]

For the out-of-plane translations ΔZ in a single-camera system, the resulting displacement and strain field can be written as follows:

$$\begin{aligned} U(\Delta Z) &\approx x_s(\frac{\Delta Z}{Z}) \\ V(\Delta Z) &\approx y_s(\frac{\Delta Z}{Z}) \end{aligned} \tag{2.39}$$

$$\begin{aligned} \varepsilon_{xx} &= \frac{\partial U(\Delta Z)}{\partial x_s} \approx \frac{\Delta Z}{Z} \\ \varepsilon_{yy} &= \frac{\partial V(\Delta Z)}{\partial y_s} \approx \frac{\Delta Z}{Z} \end{aligned} \tag{2.40}$$

The result indicates that out-of-plane translation would decrease image magnification and introduce a negative normal strain in all directions. It's important to note that by employing a more complex lens system such as a telecentric lens system, the effect of out-of-plane motion can be reduced by replacing physical object distance with a many times larger virtual distance.

For the out-of-plane rotation θ, the resulting displacement and strain field can be written as follows:

$$\begin{aligned} U(\Delta Z) &\approx \frac{L}{Z} X\left(\frac{Y\sin\theta}{Z}\right) \\ V(\Delta Z) &\approx \frac{L}{Z} Y\left(\cos\theta\frac{Y\sin\theta\cos\theta}{Z}\right) \end{aligned} \tag{2.41}$$

$$\begin{aligned}\varepsilon_{xx} &= \frac{\partial U(\Delta Z)}{\partial x_s} \approx \frac{Y\sin\theta}{Z} \\ \varepsilon_{yy} &= \frac{\partial V(\Delta Z)}{\partial y_s} \approx \cos\theta\frac{Y\sin(2\theta)}{Z}\end{aligned} \tag{2.42}$$

The result indicates that out-of-plane rotation would introduce unequal negative normal strains in x_s and y_s directions that are functions of both the rotation angle θ and offset position from the rotation axis.

Theoretically, out-of-plane motions are not avoidable and the best choice seems to be minimizing the error in measurements introduced by out-of-plane motion, where the employment of a 3D-DIC system would offer a useful alternative.

2.10.3. Reconstruction Errors

In the 3D-DIC technique, there is a necessary procedure that transforms the coordination of a certain image point in each camera system into the general 3D coordination system. This is called the reconstruction. However, systematic errors would appear in this process for each reconstructed point there are both reconstructed coordinates $[X_n, Y_n, Z_n]$ and associated true coordinates $[X_n^{(t)}, Y_n^{(t)}, Z_n^{(t)}]$:

$$\begin{aligned}\Delta X_n &= X_n - X_n^{(t)} \\ \Delta Y_n &= Y_n - Y_n^{(t)} \\ \Delta Z_n &= Z_n - Z_n^{(t)}\end{aligned} \tag{2.43}$$

The mean error ε_M and the Root Mean Square (Root Mean Square (RMS)) ε_R can be defined as:

$$\varepsilon_M = \frac{1}{N}\sqrt{(\sum_{n=1}^{N}\Delta X_n)^2 + (\sum_{n=1}^{N}\Delta Y_n)^2 + (\sum_{n=1}^{N}\Delta Z_n)^2} \tag{2.44}$$

$$\varepsilon_R = \sqrt{\frac{1}{N}\sum_{n=1}^{N}(\Delta X_n)^2 + (\Delta Y_n)^2 + (\Delta Z_n)^2} \tag{2.45}$$

In 3D-DIC software like MultiDIC, such errors are computed for further analysis and minimizing attempt.

2.11. Uncertainty

There exists uncertainty in static strength measurement, both in the deviation of apparatus data reading and in DIC measurement. A comprehensive way to measure the effects of uncertainty is to introduce probabilistic analysis into the experiment. For the reliability of the data set the term *confidence interval* can be adopted which shall be defined as below:[26]

Confidence Intervals

Given a dataset $x_1, ..., x_n$ modeled as realization of random variables $X_1, ...X_n$, for the parameter of interest θ if there are sample statistics $L_n = g(X_1, ..., X_n)$ and $U_n = h(X_1, ..., X_n)$ such that:

$$P(L_n < \theta < U_n) \geq \gamma \tag{2.46}$$

where γ is the probabilistic number between 0 and 1, then $l_n = g(x_1, ...x_n)$ and $u_n = h(x_1, ..., x_n)$ is called a $100 \times \gamma\%$ **confidence interval** for θ, and the number γ is often referred to as **confidence level**. The corresponding range of the parameter is called the **confidence bound (Confidence Bound (CB))**.

Likelihood and loglikelihood

Given a dataset $x_1, ..., x_n$ modeled as the realization of a random sample from a distribution characterized by a parameter θ, write $p_\theta(x)$ as the probability mass function and $f_\theta(x)$ for a discrete distribution as the probability density function for a continuous distribution, the likelihood function can be expressed respectively as:

$$L(\theta) = P(X_1 = x_1, ..., X_n = x_n) = p_\theta(x_1)\cdots p_\theta(x_n) \tag{2.47}$$

$$L(\theta) = f_\theta(x_1) f_\theta(x_2)\cdots f_\theta(x_n) \tag{2.48}$$

For the given dataset, if a set of values $t = h(x_1, x_2, ..., x_n)$ which maximizes the likelihood function $L(\theta)$, the corresponding random variable $T = h(X_1, X_2, ..., X_n)$ is called the **maximum likelihood estimator (Maximum Likelihood Estimator (MLE))** for θ.

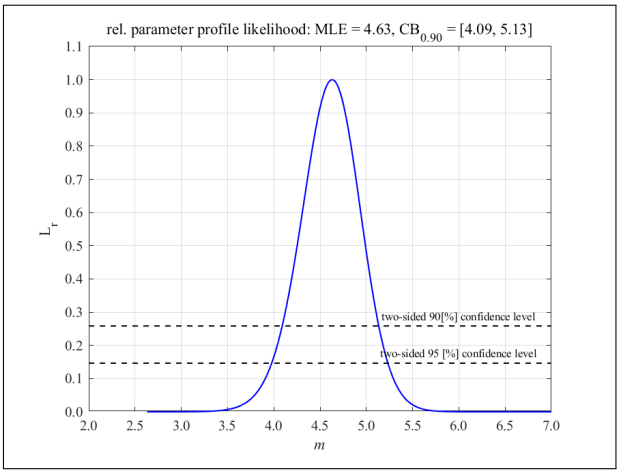

Figure 2.14: An example of the confidence interval and MLE in the practice of fatigue life estimation[26]

Usually one can find the maximum by differentiating the likelihood function $L(\theta)$. Due to the fact that $L(\theta)$ is a product of terms involving θ, taking the derivative of it requires the product rule from calculus. To simplify the differentiating one can change the product of the terms involving θ into a sum of logarithms of these terms, defined as:

$$l(\theta) = \ln(L(\theta)) \tag{2.49}$$

Because the monotonicity of the function remains unchanged, $l(\theta)$ and $L(\theta)$ can attain their extreme values for the same values of θ.

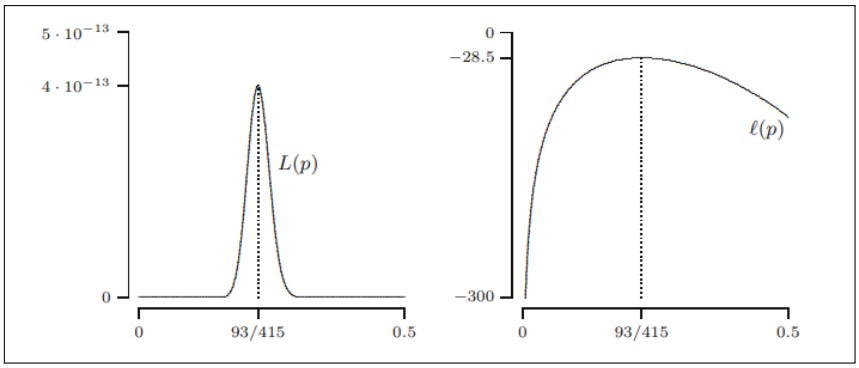

Figure 2.15: An example of likelihood can loglikelihood function

2.12. Concluding Remarks

This chapter summarized the literature review on both the static material properties and digital image correlation. Based on the literature study conclusions can be made:

1. For the measurement of Yield Strength **Offset Method** is preferred in this case, in light of the material structure which lacks existing stress-strain characteristics.

2. A priori analysis is necessary to guarantee the image texture quality, and further ensure the quality of displacement measurement. Criteria need to be taken into account including the effective range of the graylevel distribution, relative fluctuations as well as correlation radii.

3. Both global and local DIC method is available for use for the measurement of the displacement field, while for the global method a modified **ALDIC** method is recommended which improves the convergence of iterative process and compatibility between displacement and displacement gradient. For

local DIC a reliability-guided formulation **RG-DIC** is recommended which optimizes the computation path of conventional local DIC. Formulation performance needs further comparison throughout the experiment.

4. For the measurement of elastic material properties along with the material zone boundaries confidence bound is expected to be established with a commitment to scientific rigor.

3

Experiment and Simulation Setup

3.1. Aim and constraints

The experiment was designed in order to obtain the **displacement field** of the ROI on the specimen surface under different load levels within the elastic region. The applied specimen dimension is as depicted in Figure 3.2, with a length of $400mm$ in total and width of $6mm$. The DIC analysis will be conducted on the cross-section in the length-width plane. The experiment aims to achieve the following objectives:

1. There should be a sufficient number of image sets taken at each load level to establish a confidence interval and minimize the impact of random errors;

2. The experiment focuses on the static behavior of the structure; therefore, the number of load cycles should be kept low to avoid fatigue behavior;

3. The speed of testing should be limited under a certain level to guarantee the accuracy of data acquisition by the machine;

4. The experiment is concerned with the elastic behavior of the structure. Therefore, a preliminary estimate should be made to prevent plastic behavior.

Based on the targets above the experiment set-up can be determined.

3.2. Tensile test experiment setup

This thesis aims to obtain the elastic mechanical properties of FSW joints, for which the data sets shall be collected with the tensile test.

The general experiment setup is shown in Figure 3.1, with a sketch of the configuration. Due to the 2D DIC test, only one camera is positioned, and it must be perpendicular to the surface of the structure to ensure proper calibration. The surface has been sprayed with black and white textured coating in priori to generate the gray-level texture to be analyzed by the DIC algorithm. To make sure that the texture can be clearly identified by the camera a flashlight has been installed to enhance image visibility.

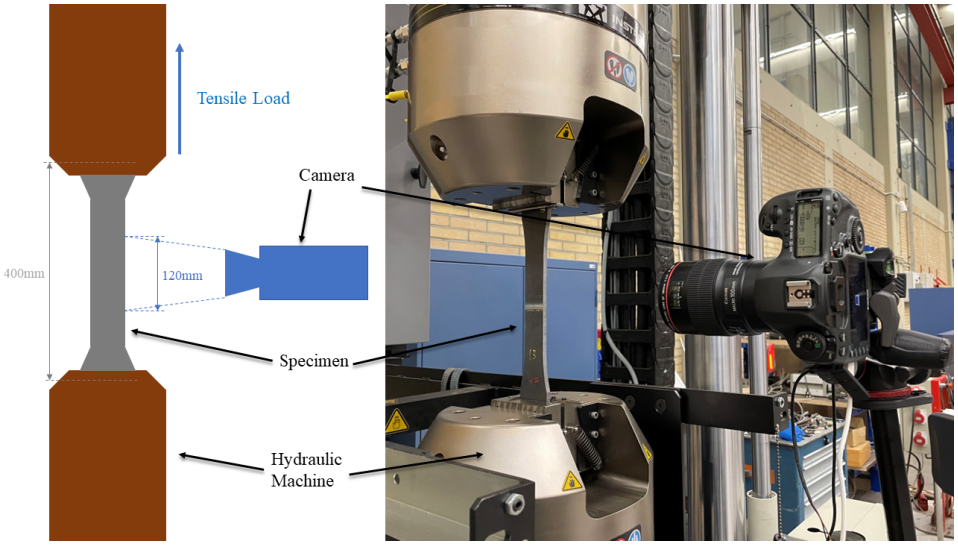

Figure 3.1: Sketch of the tensile test set-up

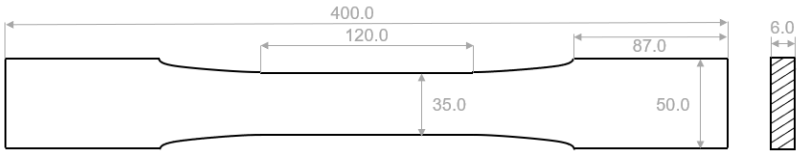

Figure 3.2: Specimen Dimension

3.2.1. Speed of testing

To guarantee the accuracy of load and strain readings limitations should be made for speed of testing. According to the recommendation from ASTM[5], any convenient speed of testing shall be used up to one-half the specified yield strength. In case this point has been reached, there is a limit of 1/16 per min per inch (approximately 51$[kN/s]$ in this case) of reduced section for the free-running rate of separation of the cross-heads. In this case, the speed of loading is set as 21$[kN/s]$ which satisfies the limitation.

3.2.2. Loading conditions

As previously mentioned, probabilistic analysis is anticipated in this thesis, requiring cyclic loading in the experiment. The preliminary plan is to apply axial loading to the specimen 3 cycles for each load level, where for each loading 5 pictures will be taken. As to the reference image, it should be chosen from the unloading time after a certain load level to minimize accumulated errors. Additionally, for each loading cycle 5 reference images will be taken, to investigate the influence on the measurement from the choice of reference images, DIC tests were conducted between different reference images. The average measured displacement between reference images turned out to be around 0.005$[pixels]$ (including rigid body motion). Compared with the average value of 13$[pixels]$ between the reference image and the deformed image, the difference in the choice of the reference image is negligible. Hence, only 1 out of 5 reference images will be chosen for the following research.

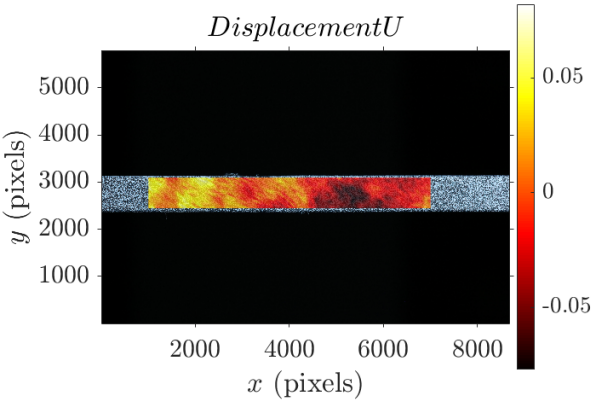

Figure 3.3: Typical difference in displacement field U_x measured by DIC between reference images

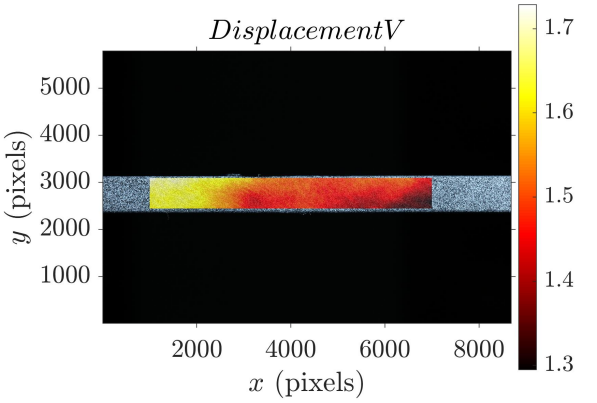

Figure 3.4: Typical displacement field U_x measured by DIC between reference and deformed image under $F_x = 21kN$

As a result, for each load level, $3 \times 5 = 15$ groups of data will be recorded to establish the confidence interval. In addition, 5 images will be recorded before all the loading conditions (before $t = 0$ in figure 3.5) as a reference.

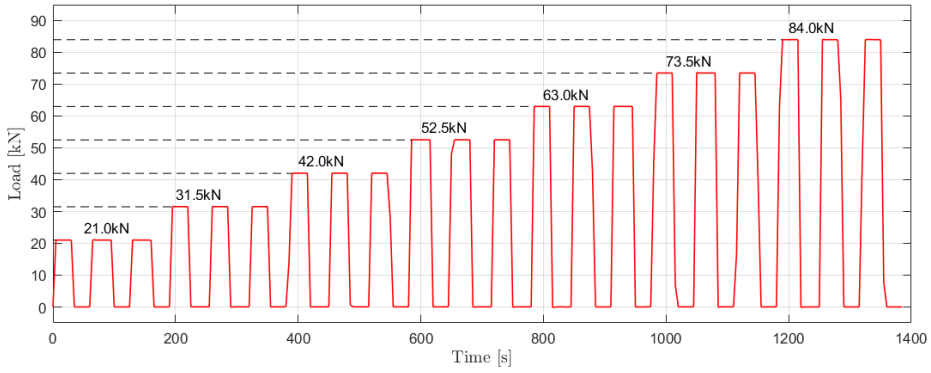

Figure 3.5: Experiment loading condition

3.3. FEM Simulation Setup

Apart from tensile test and DIC analysis, Finite element simulation will also be applied in this thesis. Through the comparison between it and DIC, the most likely value of Young's Modulus along with the boundary lines of the weld nugget zone can be determined.

Due to the fact that in the present case, a 2D DIC test is adopted, a 2D FEM model will also be applied. The element type **PLANE182**, which is a type of quadrilateral 4-node element usually used for modeling structures where bending and membrane effects are significant. Plane stress is assumed on account that for each loading condition, the stress remains unchanged. In this thesis, FEM is used mainly to distinguish between Base Material Zone (Base Material Zone (BMZ)) and Weld Nugget Zone (Weld Nugget Zone (WNZ)), so only two types of material were defined. The initial guess of the weld nugget boundary lines is based on the photo of an etched cross-section of the structure specimen (as in Figure3.6). Mapped mesh is adopted in the FEM model to guarantee the accuracy and convergence.

Figure 3.6: A close-up view of the etched cross-section of the specimen surface

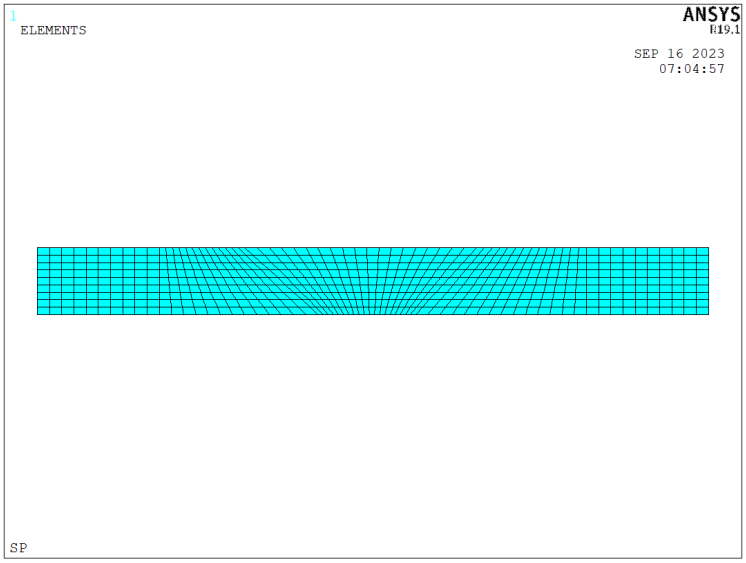

Figure 3.7: Finite element mesh adopted in this case(with initially guessed WNZ boundary lines

As for the boundary condition, a clamped constraint is applied on the left-hand side and the load is applied on the right-hand side. It shall be noted that because only a local range of the specimen surface (the longitudinal length of ROI being approximately 60$[mm]$) out of the whole length is being processed by DIC, the modeling of FEM also follows the same dimension, while in following comparison the nodes on the constraint side would be subtracted in order to reduce the systematic errors. There exists unit conversion between the result of FEM (in $[mm]$) and DIC (in $[pixels]$) as well, which shall be taken into account in the final comparison procedure.

3.4. Concluding Remarks

This chapter reviewed the basic setup for the experiments and simulations of the project, including the tensile test configuration, determination of DIC parameters based on the texture quality analysis, and pre-analysis settings of FEM simulation. Points worth noting include:

1. In the tensile test there are 7 load levels:
   $100[MPa], 150[MPa], 200[MPa], 250[MPa], 300[MPa], 350[MPa], 400[MPa]$.
   For each load level, the loading is repeated for 3 cycles during every 5 images taken for the DIC test. So in total $7 \times 3 \times 5 = 105$ groups of data are available for the DIC test to establish the static material properties. In loading of around $400[Mpa]$ there is expected to be plastic behaviors happening which needs additional attention.

2. For the finite element simulation an initial guess of the WNZ boundary line location is used as input based on the photo of the etched cross-section. A more specific location shall be determined in the post-analysis process by comparing the displacement field of FEM and DIC.

4

DIC analysis

4.1. Texture Quality

Before applying DIC formulations, *a priori* analysis is required to estimate the texture quality determined DIC displacement measurement performance, for which both global and local indicators will be introduced.

The texture quality evaluation is based on the artificial texture on the specimen surface which is covered by white (by spray can) and black (by airbrush system). The specified region of interest as well as the texture close-up is shown in Figure 4.1, Figure 4.2, and Figure 4.3 below.

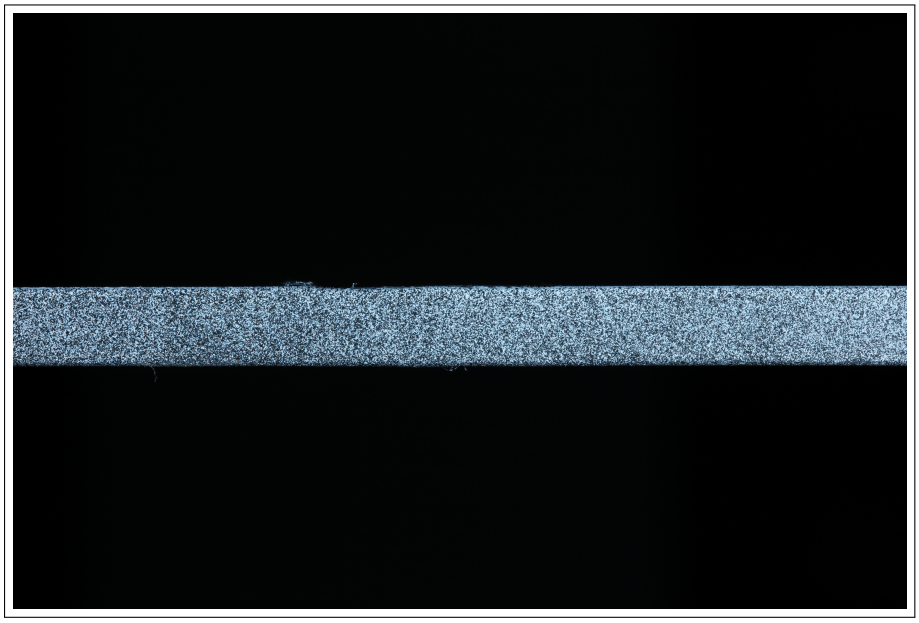

Figure 4.1: Typical texture in DIC reference image

To guarantee that each subset contains enough information for further analysis the indicator shall be evaluated for subsets with different scales. In this case, subsets of $50\times50[pixels]$, $100\times100[pixels]$, $200\times200[pixels]$ and the whole ROI will be analyzed.

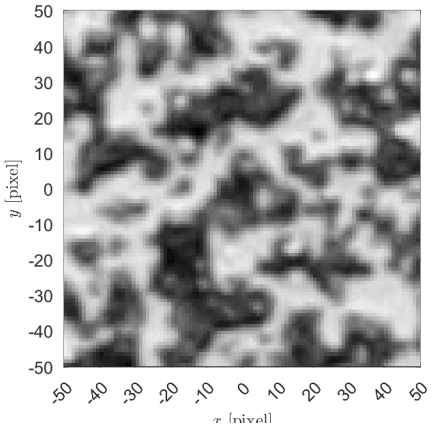

Figure 4.2: Typical texture close up at BMZ region ($100 \times 100[pixels]$) in reference image

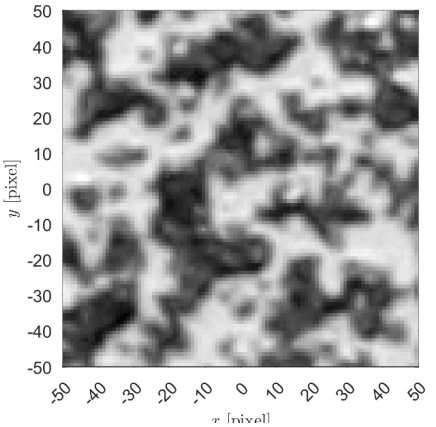

Figure 4.3: Typical texture close up at BMZ region ($100 \times 100[pixels]$) in deformed image

A global indicator for the texture quality is the grey level distribution histogram, which describes the uniqueness of the pixel combination for the chosen ROI.

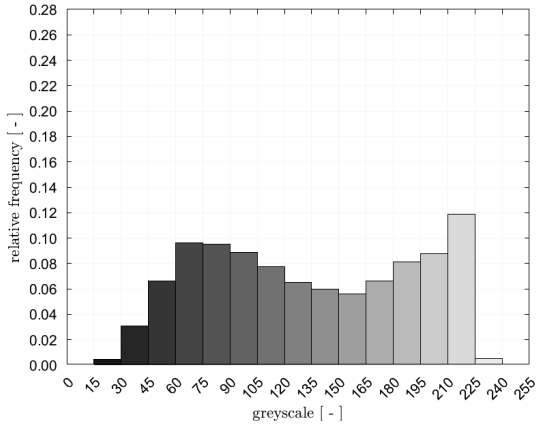

Figure 4.4: Typical grey level distribution histogram ($50 \times 50[pixels]$)

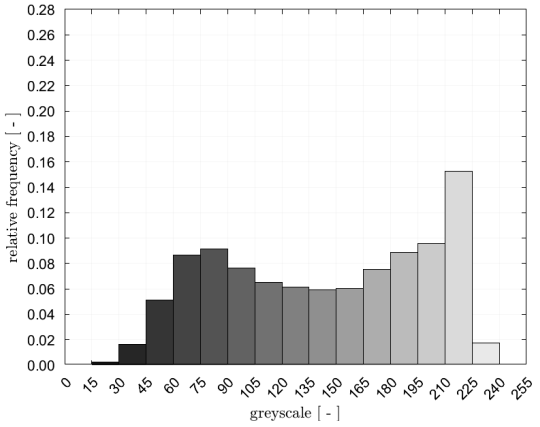

Figure 4.5: Typical grey level distribution histogram ($100 \times 100[pixels]$)

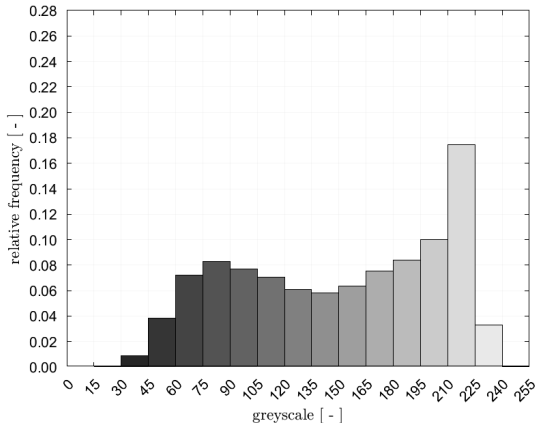

Figure 4.6: Typical grey level distribution histogram ($200 \times 200[pixels]$)

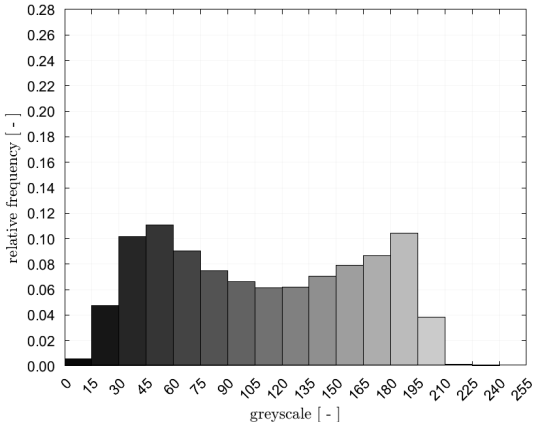

Figure 4.7: Typical grey level distribution histogram (the whole ROI)

In the present case, the dynamic range of the camera is wide enough (i.e., ca. 225 grey levels)to ensure the uniqueness for subsets at least in the scale of $50 \times 50[pixels]$. And there is almost no pure saturation (grey level = 255) nor pure reflection (grey level = 0) appearing, indicating that the subset grey level is robust enough for further analysis and the random error in deformation measurement can be reduced.

As for the local quality and sensitivity indicator, the subset grey level standard deviation can be applied either to evaluate whether the subset contains enough information to describe a unique displacement field or to give a preliminary estimate of the appropriate window size for DIC analysis [7].

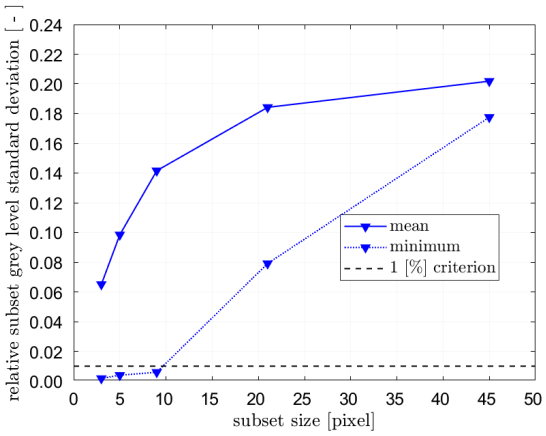

Figure 4.8: Typical subset grey level standard deviation

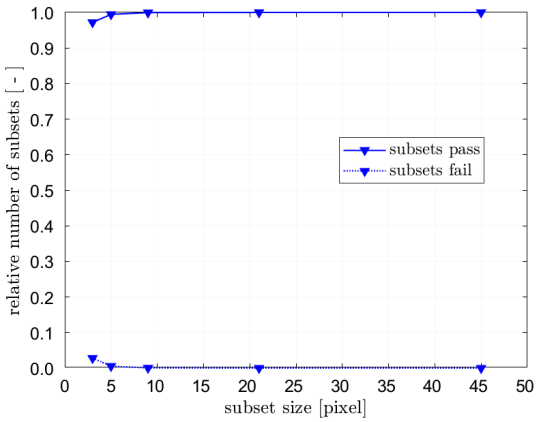

Figure 4.9: Typical subset grey level standard deviation pass criterion

As discussed in the literature review, there is a criterion of 1% of the dynamic range of the camera below which the gradients are considered to be not enough to capture the displacements. From Figure 4.8 and Figure 4.9 it can be concluded that subsets with a scale of larger than $8[pixels]$ can be regarded as large enough for deformation field description.

In addition, there is another local indicator known as correlation radii which can be adopted to estimate the security of convergence.

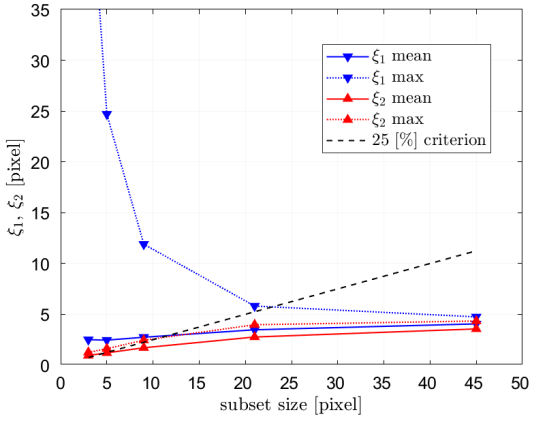

Figure 4.10: Typical subset correlation radii for different sizes

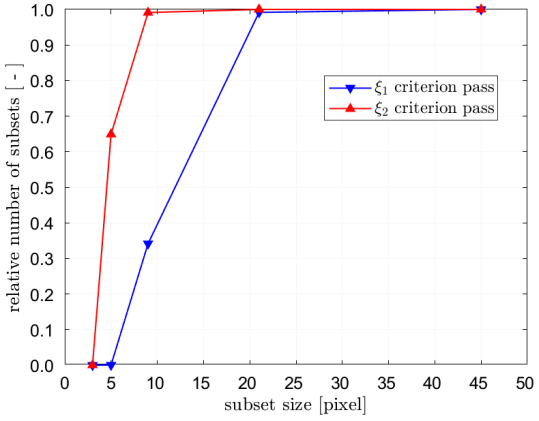

Figure 4.11: Typical subset correlation radii pass criterion

Recall the literature review, there is a practical limit of 25% of the element size that shall be satisfied for both ξ_1 (in the x direction) and ξ_2 (in the y direction). In this case, both the mean and maximum value of correlation are evaluated. It can be concluded from Figure 4.10 and 4.11 that if considering the mean value, subsets

with a size of up to 16[$pixels$] are large enough to give an accurate measurement. However, for the sake of conservatism subsets with 32[$pixels$] are recommended. There is also information that the slopes of the two correlation radii are different, especially in the case of smaller subset sizes, which indicates the anisotropic characteristic of the texture[27].

As a result, for further DIC analysis, the subset/window size is suggested to be $32 \times 32[pixels]$ or larger to ensure security.

4.2. ALDIC

In the literature review, there is a remark that both local and global DIC algorithm is applicable in this experiment, while for global DIC ALDIC algorithm is recommended and for local DIC RG-DIC algorithm is recommended. However, the comparison in the literature review is based on the mathematical theory and different models, quantitative and comprehensive comparison is a significant engineering application. In this chapter, the analysis result of ALDIC with automatically generated rectangular mesh and user-defined trapezoid mesh (same mesh with FEM) will be compared with that applying RG-DIC (local algorithm) and Correli (another global DIC algorithm as reference) to conclude which method is best suitable for use in this study.

The key idea of ALDIC is to treat the constraint which describes the compatibility between displacement **u** and displacement gradient **F** efficiently. Additional penalty terms were added to the correlation calculation including Lagrange multipliers and real scalars. Here an open-source program pf ALDIC algorithm named JYang is employed.

As it comes to application, ALDIC used *Lagrangian* description which tracks each node with its initial position in the reference configuration and its current position in the deformed configuration. To make the coordinate system used by different DIC algorithms to describe the displacement field consistent when using ALDIC it's recommended to select the reference image as the second image while the deformed image as the first image.

As a global DIC algorithm, ALDIC allows user-defined finite element mesh as input, the 3 versions of code require respectively automatically generated rectangular mesh, self-defined quadrilateral mesh, and self-defined triangle mesh. In this thesis, due to the cross-section surface properties, the first two methods are adopted and compared.

In global DIC the window size which decides the size of the search range used for tracking and comparing patterns needs to be defined before the test. In texture quality analysis a recommendation has been given which uses window sizes of 32 pixels. Apart from that an initial guess search zone needs to be given beforehand which defines the probably largest displacement in this correlation. This parameter serves as a low pass filter which could subtract the illogical noise data. So a relatively small value should be adopted at first and enlarged gradually until a convincing displacement field is generated. It shall be noted that for the DIC test only a local part of the specimen is being analyzed which implies rigid motion is included in the displacement measurement, this should be taken into account when defining the initial guess search zone.

For both the DIC using rectangular mesh and Q4 mesh the ROI should be kept unchanged. And for the Q4 mesh the mesh used in the FEM test is adopted. The result from Q4 mesh are as shown from Figure 4.12 to Figure 4.18.

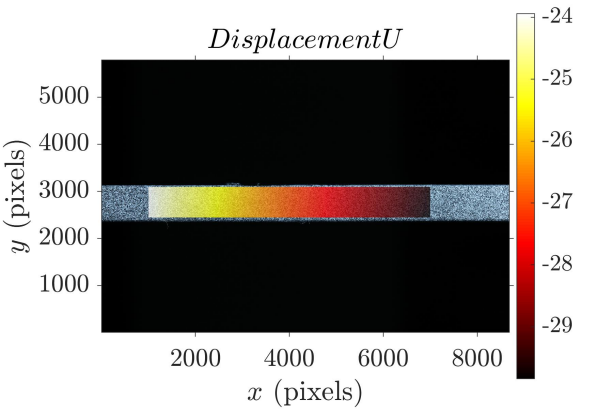

Figure 4.12: Typical ALDIC displacement fields - U_x including rigid body motion (Using trapezoid mesh)

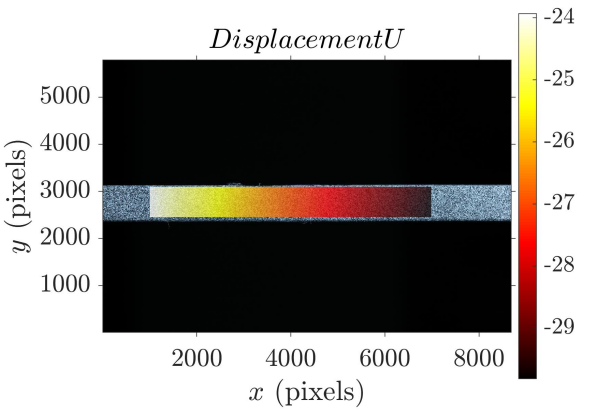

Figure 4.13: Typical ALDIC displacement fields - U_x including rigid body motion (Using rectangular mesh)

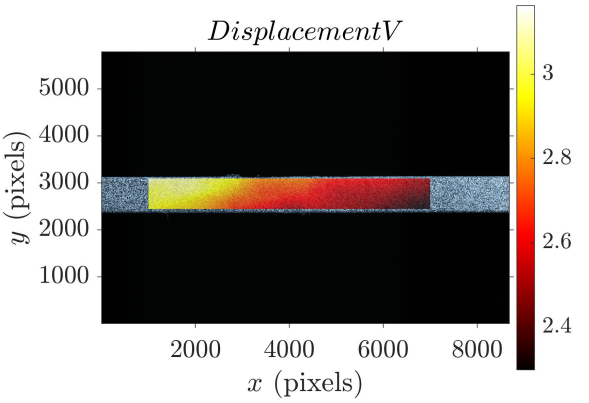

Figure 4.14: Typical ALDIC displacement fields - U_y including rigid body motion (Using trapezoid mesh)

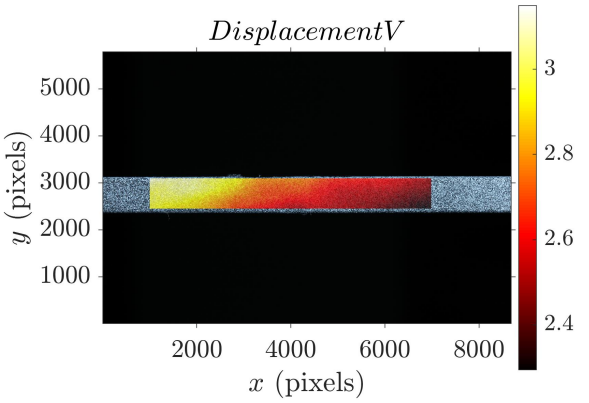

Figure 4.15: Typical ALDIC displacement fields - U_y including rigid body motion (Using rectangular mesh)

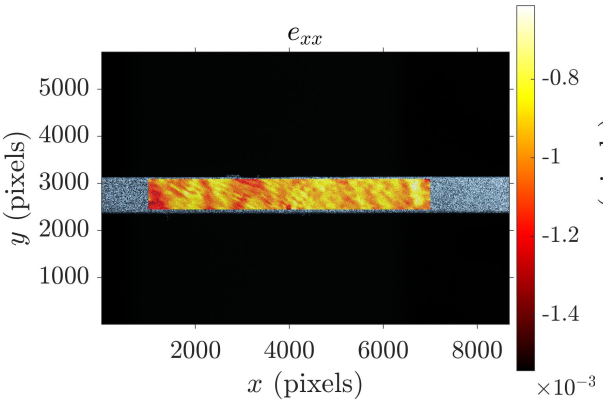

Figure 4.16: Typical ALDIC strain fields - ϵ_{xx} (Using trapezoid mesh)

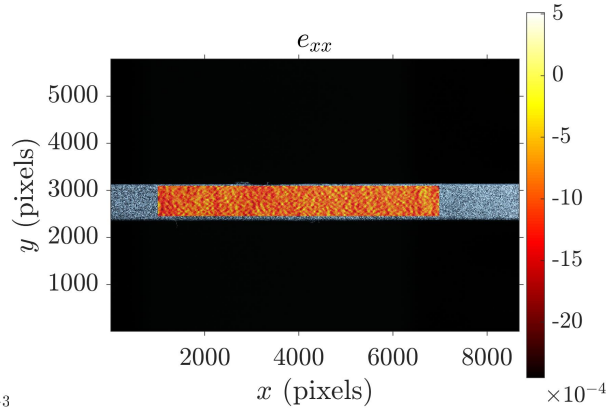

Figure 4.17: Typical ALDIC strain fields - ϵ_{xx} (Using rectangular mesh)

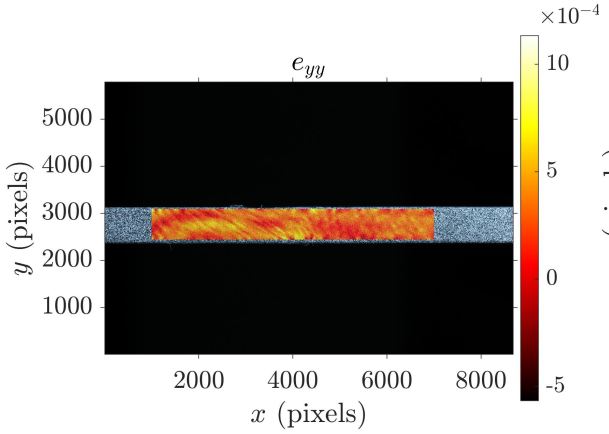

Figure 4.18: Typical ALDIC strain fields - ϵ_{yy}(Using trapezoid mesh)

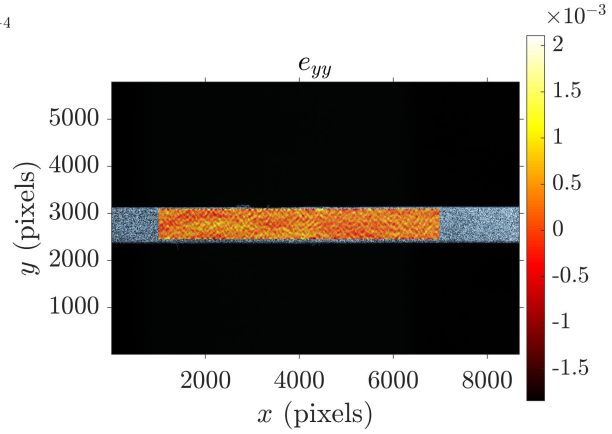

Figure 4.19: Typical ALDIC displacement fields - ϵ_{yy}(Using rectangular mesh)

From the results, it can be observed that using different meshes ALDIC gives generally similar displacement field results. However, when it comes to the strain field which includes the procedure of subtracting rigid body motion and computing strain, there exists an obvious deviation between the contour plot. And it can be easily concluded that with rectangular mesh the strain field result contains more noise data. In order to investigate the reason for that the calculation was gone through again and it's found that two aspects of the calculation would lead to the final errors: 1. The method of computing strain (using **Finite Element Method (Finite Element Method (FEM))** or **Finite Difference Method (Finite Difference Method (FDM))**; 2.The method of strain field description (**Infinitesimal strain** or **Eulerian strain** or **Green-lagrangian strain**). In this case, strain is computed by **FEM** and described by **Infinitesimal strain**. The difference in the methods of computing and describing the strain was investigated.

4.2.1. Strain Computation

The difference between FEM and FDM lies mainly in the numerical approach employed to compute and solve partial differential equations in specific problems. FDM, usually suitable for structured grids, discretizes the equation by approximating derivatives at the grid nodes between physical entities[28][29]. While FEM, more flexible in modeling complex and irregularly shaped geometries, tends to find the optimized basis functions by minimizing the potential energy of the system[30][31][32]. From the comparison between Figure 4.20 and Figure 4.21.

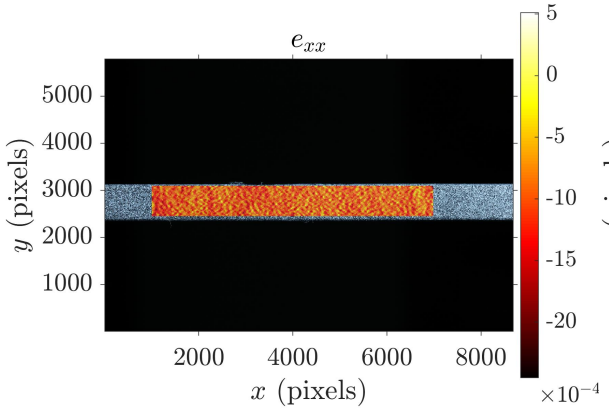

Figure 4.20: Strain field ϵ_{xx} computed using Finite Element Method (Infinitesimal strain)

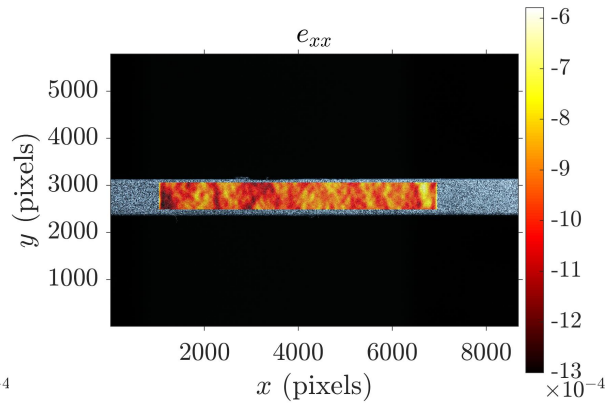

Figure 4.21: Strain field ϵ_{xx} computed using Finite Difference Method (Infinitesimal strain)

The infinitesimal strain theory assumes that deformations are small compared with the length of the whole

structure, and the rotational angles between material points are negligible which means rotational rigid body motion are respectively small. The strain field under the infinitesimal assumption is described usually by a linearized strain tensor. It is generally applied for describing structural behaviors within the elastic zone.

4.2.2. Strain Formulation

Both Eulerian and Green-Lagrangian theory are applicable for non-linear and large deformation behavior of the structure, different from infinitesimal theory. The difference in this two assumption lies in that Green-lagrangian uses the material coordinates as the frame of reference and hence is able to track the deformation of the structure, while the Eulerian description uses the spatial coordinates as the frame of reference.[33]
Eulerian Finite Strain Tensor:

$$e_{ij} = \frac{1}{2}\left(\frac{\partial u_i}{\partial x_j} + \frac{\partial u_j}{\partial x_i} - \frac{\partial u_k}{\partial x_i}\frac{\partial u_k}{\partial x_j}\right) \tag{4.1}$$

Lagrangian Finite Strain Tensor:

$$e_{ij} = \frac{1}{2}\left(\frac{\partial u_i}{\partial x_j} + \frac{\partial u_j}{\partial x_i} + \frac{\partial u_k}{\partial x_i}\frac{\partial u_k}{\partial x_j}\right) \tag{4.2}$$

In this case of 2D linear structure behavior, there is expected to be no deviation between the description of Eulerian and Green-Lagrangian theory. To better illustrate which method provides a better performance comparisons are made between results using different methods respectively. A quantified index of the standard deviation, which can indicate the level of stochasticity of the data is presented.

	Infinitesimal	Euler	Green-Lagrange
FEM	2.62×10^{-4}	2.62×10^{-4}	2.62×10^{-4}
FDM	9.14×10^{-5}	9.14×10^{-5}	9.14×10^{-5}
FEM(mapped mesh)	1.24×10^{-4}	1.24×10^{-4}	1.24×10^{-4}

Table 4.1: Comparison between different methods of computing and describing strain - strain field standard deviation

It can be concluded that the difference in the description method of the strain field leads to no difference as discussed. But for the computational method, FDM provides results with lower stochasticity than FEM when both use brutally rectangular mesh, which comes mainly from the higher requirement on the quality of the mesh. Improvement in the accuracy can be achieved by using mapped (self-defined quadrilateral) mesh on FEM.

4.3. RG-DIC

Different from the methods above, RG-DIC is a local DIC algorithm that requires no input of finite element mesh and uses a seed point to determine the computation route instead. Here an open-source RG-DIC algorithm named Ncorr is employed. The subset radius is set as $32[pixels]$ to keep in line with the settings of ALDIC. Typical results of RG-DIC is as shown from Figure 4.22 to Figure 4.25.

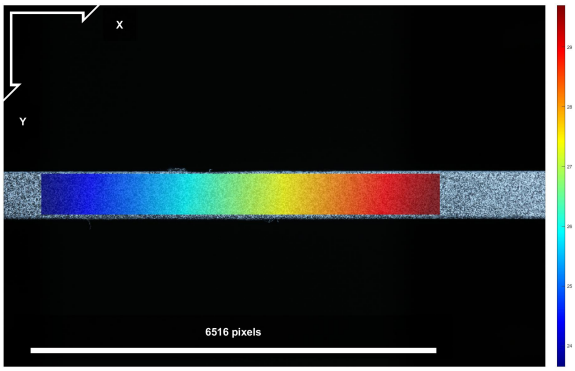

Figure 4.22: Typical RG-DIC displacement field - U_x including rigid body motion

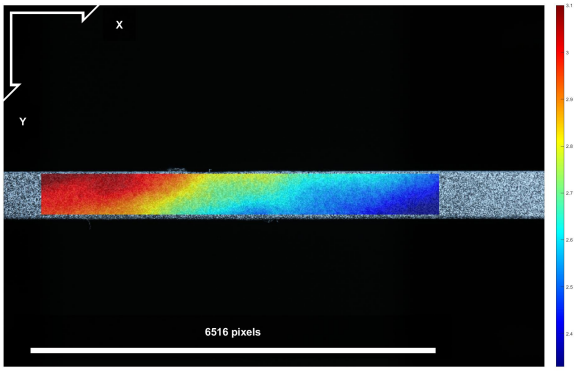

Figure 4.23: Typical RG-DIC displacement field - U_y including rigid body motion

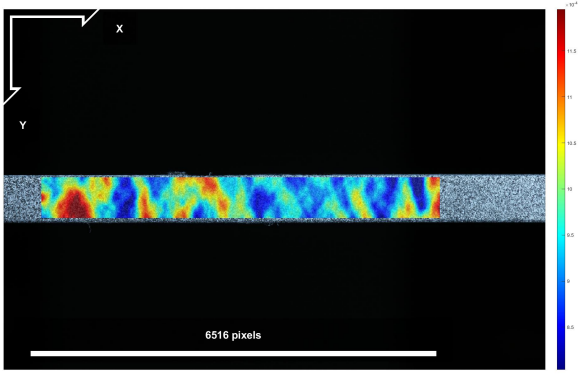

Figure 4.24: Typical RG-DIC strain field - ϵ_{xx}

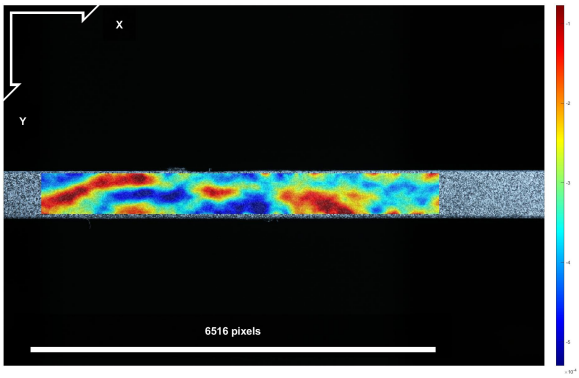

Figure 4.25: Typical RG-DIC strain field - ϵ_{yy}

4.4. DIC-FEM displacement field comparison

The ultimate goal of applying the DIC algorithm is to obtain an accurate measurement of the displacement and strain field of the specimen, to compare it with the results by FEM, and determine the elastic properties along with the location of weld nugget zone boundary lines. On account of that the comparison result between different DIC methods and FEM shall be employed as a criterion of evaluating algorithm performance.

Before carrying out the comparison the effect of rigid body should be subtracted at first. In the matter that for FEM the surface to be analyzed is modeled as a 2D plane and the boundary condition is applied directly to the side of it, the left-hand side of the FEM model is regarded as fixed while in the experiment it's not. As a result, the displacement of the left-hand side nodes shall be subtracted from the whole displacement field to make a comparison in a unified coordinate system. For the translational rigid body motion, it can be removed by taking derivatives of the displacement tensor in a certain direction and integrating them after setting the original position of the reference point. In this case, the nodes on the left-hand side of the ROI are set as reference points. For the rotational rigid body motion, it's assumed in this case that the structure moves by a fixed angle which means that the influence from bending moment and torsion is limited.

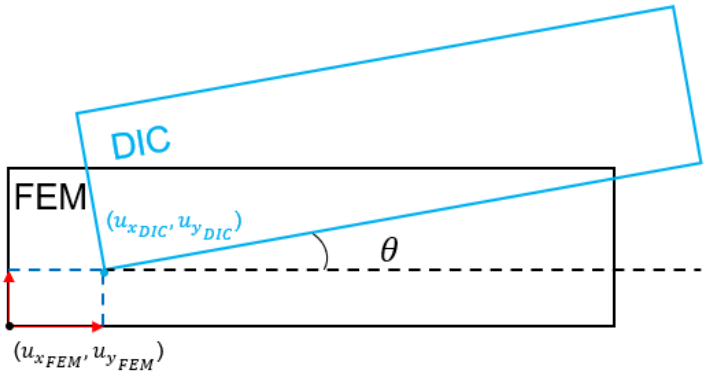

Figure 4.26: The effect on the assumption of constant translational and rotational rigid body motion

After subtracting the rigid body motion a quantitative comparison was made between DIC and FEM results. Note that for different DIC algorithms, the mesh describing the displacement field varies as well. Here the MATLAB command *scatteredInterpolant* is adopted to perform the interpolation, with the mesh density following the lowest requirement of texture quality analysis result.

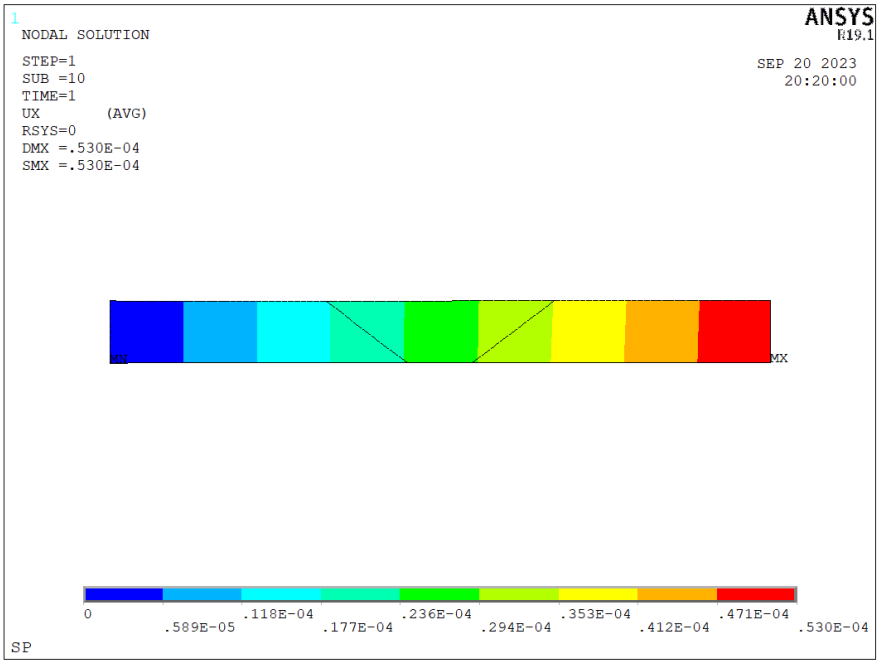

Figure 4.27: Typical FEM result displacement field U_x

FEM result describes the ideal physic model under axial loading conditions, which means continuous and noise-free data. Besides the ALDIC and RG-DIC discussed above, the result from global DIC algorithm **Correli** is also used for comparison, which provides unfiltered results that can be used as reference.

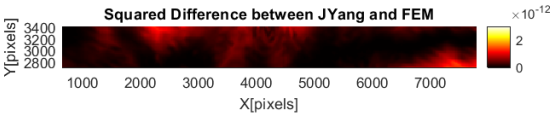

Figure 4.28: Squared difference of displacement U_x field between ALDIC(trapezoid mesh) and FEM result

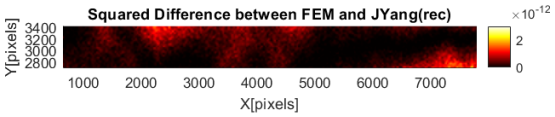

Figure 4.29: Squared difference of displacement U_x field between ALDIC(rectangular mesh) and FEM result

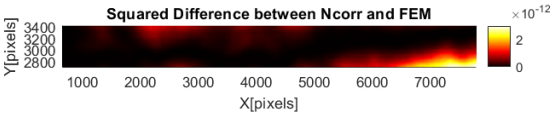

Figure 4.30: Squared difference of displacement U_x field between RG-DIC and FEM result

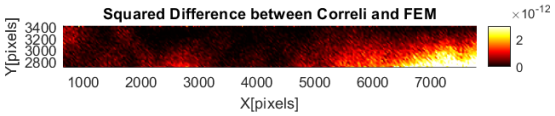

Figure 4.31: Squared difference of displacement U_x field between Correli and FEM result

From Figure 4.28 to Figure 4.31 the node-wise squared difference between DIC and FEM in displacement U_x is presented. These figures show that the three DIC algorithms generally provide similar results for the distribution of the displacement field, with a noticeable difference, primarily in the lower-right portion of the contour. Considering that in the original FEM test, the settings for Young's modulus remain the same in BMZ and WNZ and that at the right-hand side, the displacement measures by DIC is smaller than that simulated by FEM, it can be speculated that Young's modulus of BMZ in longitudinal direction should be larger than the current value adopted in FEM.

In addition, the squared difference in displacement U_y was also computed. However, from the results (Figure 4.32 to Figure 4.35) it can be observed that significant deviation exists between DIC and FEM results, except for the left-end side, where clamped boundary condition is assumed for FEM and displacements are considered to be zero to subtract rigid body motion in DIC.

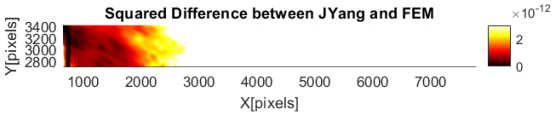

Figure 4.32: Squared difference of displacement U_y field between ALDIC(trapezoid mesh) and FEM result

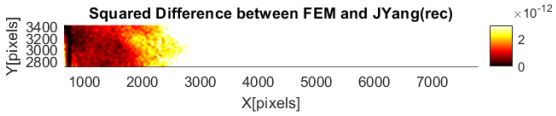

Figure 4.33: Squared difference of displacement U_y field between ALDIC(rectangular mesh) and FEM result

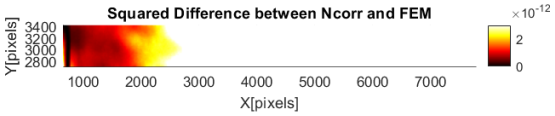

Figure 4.34: Squared difference of displacement U_y field between RG-DIC and FEM result

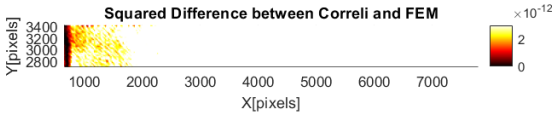

Figure 4.35: Squared difference of displacement U_y field between Correli and FEM result

The causes of the deviation, regrettably, remained unidentified throughout the course of this research. Possible contributing factors could encompass:

1. Slight tilt of the camera. Due to the fact that in DIC and FEM, the same mapped mesh was adopted, a rotational rigid body motion could exist in DIC result because of the slight tilt of the camera. Theoretically, this can be avoided by subtracting the rigid body motion from the DIC measurement result.

2. Incomplete Finite Element modeling. As mentioned in the chapter on FEM simulation setup, a 2D PLANE182 element type was assumed for FEM modeling. And only the region of interest in the DIC test was modeled in ANSYS, which means that the constraints were applied to the left-end side of the FEM model while in practice it should be on the shoulder. The deviation on the constraint point would make the FEM exhibit a higher displacement in the y direction. This problem can be investigated through complete 3D modeling in ANSYS in future research.

To establish a quantitative comparison, the SSD, MEAN value and Standard Deviation (STD) were calculated for the squared difference. The first two index implies the similarity between DIC and FEM result and the standard deviation indicates the accuracy.

	SSD	MEAN	STD
ALDIC(Q4 mesh)	3.1×10^{-9}	2.3×10^{-13}	2.4×10^{-13}
ALDIC(rectangular mesh)	3.3×10^{-9}	2.4×10^{-13}	2.6×10^{-13}
RG-DIC	3.5×10^{-9}	2.5×10^{-13}	4.3×10^{-13}
Correli	7.0×10^{-9}	5.0×10^{-13}	6.8×10^{-13}

Table 4.2: Comparison of squared difference in U_x field between different DIC algorithms and FEM

The result indicates that no matter in SSD, MEAN, STD, ALDIC, with self-defined Q4 trapezoid mesh, can generate the most accurate and robust result for the following post-analysis.

4.5. Concluding Remarks

This chapter discussed the performance of different DIC algorithms applied in this thesis, functioning as preparation work for the practical measurement. The aim is to evaluate the behavior of DIC methods quantitatively in accuracy, efficiency, and compatibility with FEM. In addition, in terms of the possible choice of computational method and description method of the strain field, the effects were discussed and recommendations were given.

1. Both ALDIC and RG-DIC bring improvement in the accuracy of DIC calculation compared with the conventional global DIC method.

2. When it comes to the general performance, **ALDIC**, with self-defined trapezoid mesh has shown the best performance in accuracy as well as in compatibility with FEM. It is recommended that in the following work, this algorithm should be adopted for the measurement of displacement and strain.

3. For the settings of **ALDIC** with rectangular mesh, FDM, rather than FEM should be employed as the computation method of strain field, for its robustness to the noise data and higher adaptability to mesh shape. As for the strain-description, in the present case of 2D linear structure properties, there is no difference between infinitesimal strain theory and Eulerian or Green-lagrangian strain theory.

5

Elastic Material Properties

5.1. Optimization of weld nugget zone boundary lines

Typically the partition of material zones of FSW structure can be highly detailed (as in Figure 5.1), with BMZ(PM in the figure), Heat Affected Zone (HAZ), Thermal-mechanically Affected Zone (TMAZ), WNZ and Flow arm. This can be defined by the structure nucleation size and shape, etc. In this case, we have only a picture of the etched cross-section for the experiment specimen, and no micro details available. As a result, a brutal way of material zone partition is employed which divides the material surface into only BMZ and WNZ. This way of partition served more as a reference for the mesh area partition for both the FEM model and global DIC modeling. And the methodology employed in this study, if turning out to be convincing, can be applied in future work for a more detailed partition of material zones based on DIC and FEM.

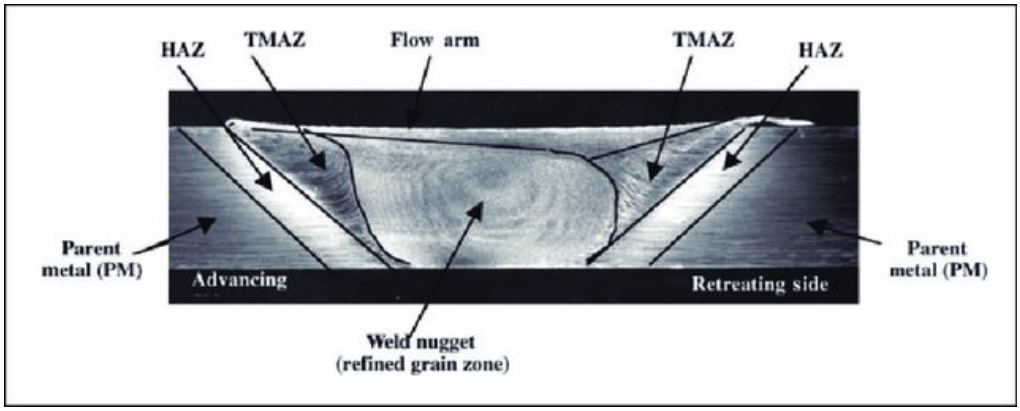

Figure 5.1: A typical way of material zone partition[34]

Figure 5.2: A qualitative way of weld nugget boundary identification based on the existing etched picture of the material surface

In this thesis, 4 parameters in total are chosen as variables to determine the boundary lines of the WNZ, which are the coordinates in the x direction of the points on the four corners. The basic assumption is made that the boundary lines are straight and thin enough. The criteria for recognizing different material zones is the elastic property of the chosen area in the longitudinal direction. For each point, there are 5 different coordinate positions to be optimized on. The optimization goal is to find the solution where the mean value of the squared difference of the displacement field U_x between DIC and FEM is minimized. This is done by coordinating ANSYS (responsible for FEM) and Matlab (responsible for DIC). The Matlab code to generate bunches of ANSYS files and complete the analysis along with the post-processing procedure is attached to the appendix.

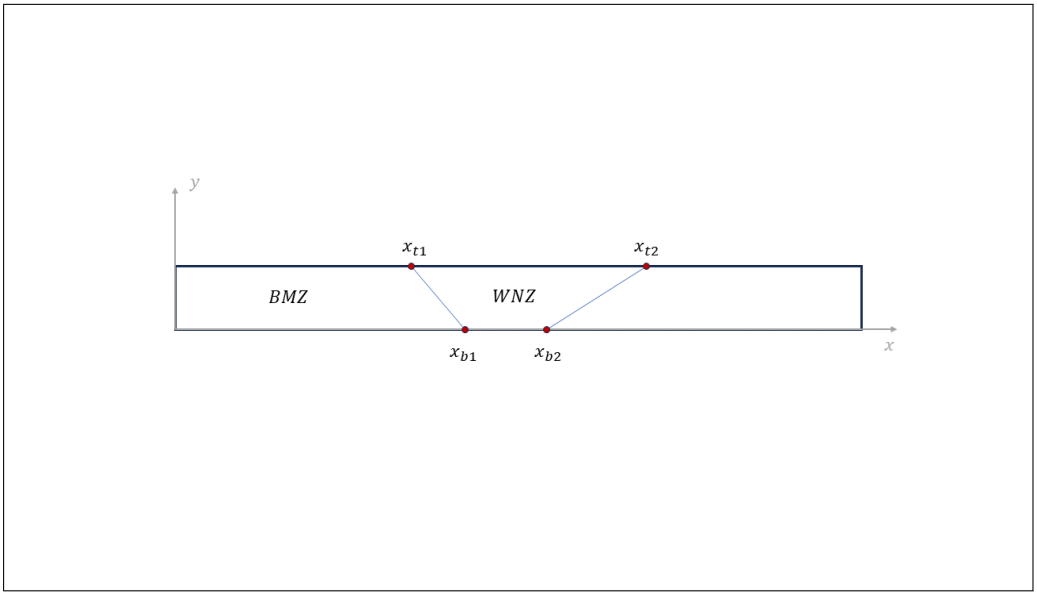

Figure 5.3: By optimizing the value of $x_{t1}, x_{t2}, x_{b1}, x_{b2}$ the boundary of different material areas can be determined

5.1.1. Optimization of the Young's Modulus for FEM model

To establish the optimization problem it is significant to make sure that the optimal solution falls within the feasible domain. Due to the fact that the FEM model is based on some ideal assumptions, the material properties of it should be slightly different from that in the real world. So the first step is to optimize Young's

modulus for the FEM model. An initial estimation was made based on a single DIC test. Since DIC is a plane stress measurement, the stress can be seen as distributed evenly on the specified cross-section. By dividing the stress by the mean value of the strain field on a certain area Young's modulus for this area can be estimated. For the preliminary partition of the material zone, a qualitative guess is made from the picture of the etched cross-section (Figure 5.1).

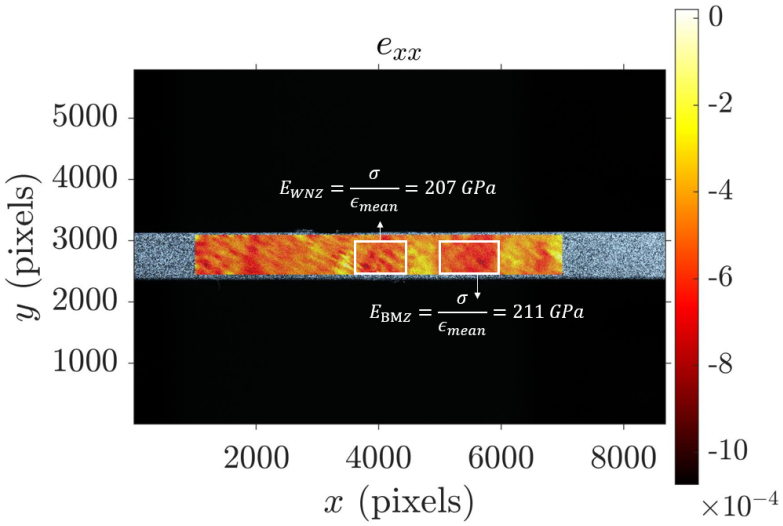

Figure 5.4: Initial Estimation of Young's modulus for different material zones

On the basis of these assumptions, the optimization of Young's Modulus was completed for each group of data. Figure 5.5 gives an example of how the target value varies with different values of E_{BMZ} and E_{WNZ}. It can be observed that the deviation between DIC and FEM is more sensitive to E_{BMZ} than to E_{WNZ} for that BMZ occupies a large proportion of the material. In further study, it is recommended to normalize the computation for both variables to make the optimization result look more intuitive.

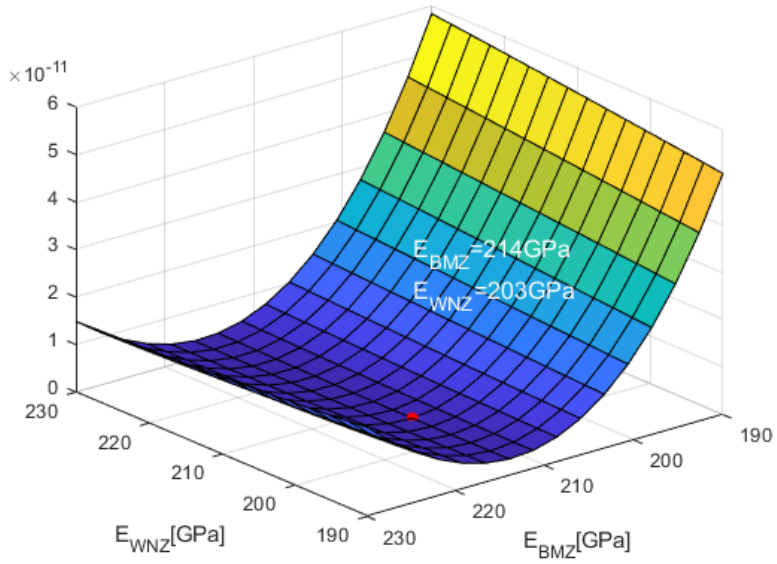

Figure 5.5: Typical result of the optimization of Young's Modulus for BMZ and WNZ

For each combination of reference image and deformation image, this optimization is carried out once. Finally, a normal distribution of Young's modulus can be given for the optimization result to give an accurate

estimation.

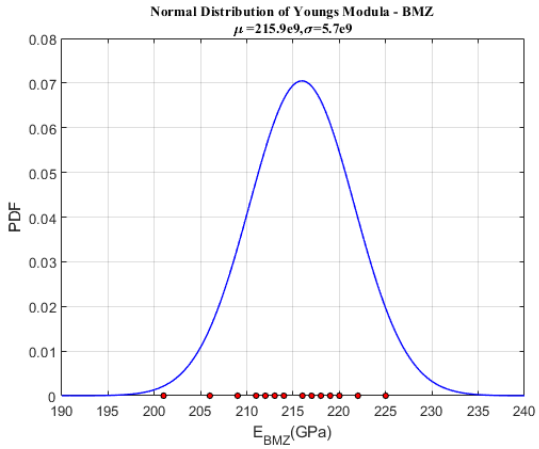

Figure 5.6: Normal distribution of the optimization result for Young's modulus in BMZ

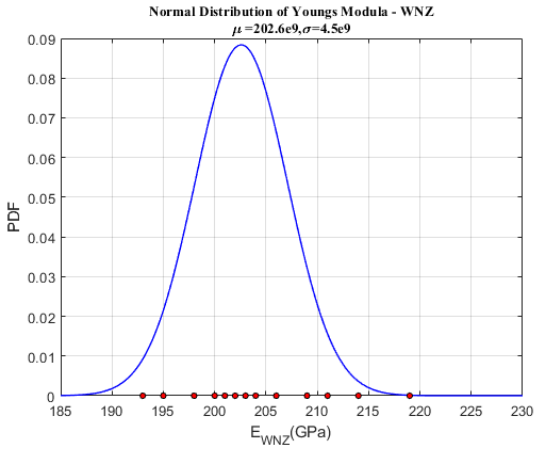

Figure 5.7: Normal distribution of the optimization result for Young's modulus in WNZ

The final result has revealed suitable values for E_{BMZ} and E_{WNZ} as input of the FEM test. $E_{BMZ} = 215.9GPa$ and $E_{WNZ} = 202.4GPa$.

5.1.2. Optimization of Weld Nugget Zone boundary lines

Once Young's modulus has been determined, the same procedure of optimization for the location of boundary lines can be implemented. For each variable, 5 different values are chosen as domain intervals. Although the discrete value interval is not large, 105 sets of data are enough to establish a credible confidence interval.

Since this is a four-variable optimization problem, the optimization curve can be plotted while keeping two of the variables constant. Following the same procedures done for the optimization of Young's modulus, the normal distribution of these 4 variables can be given.

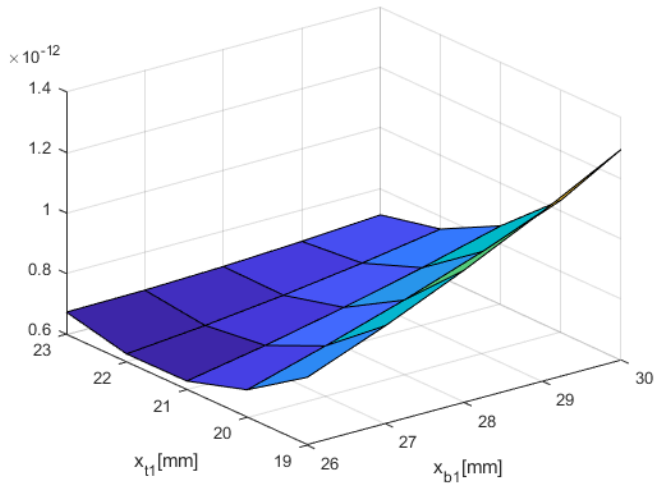

Figure 5.8: Typical surface describing the target value distribution varying with x_{t1} and x_{b1}

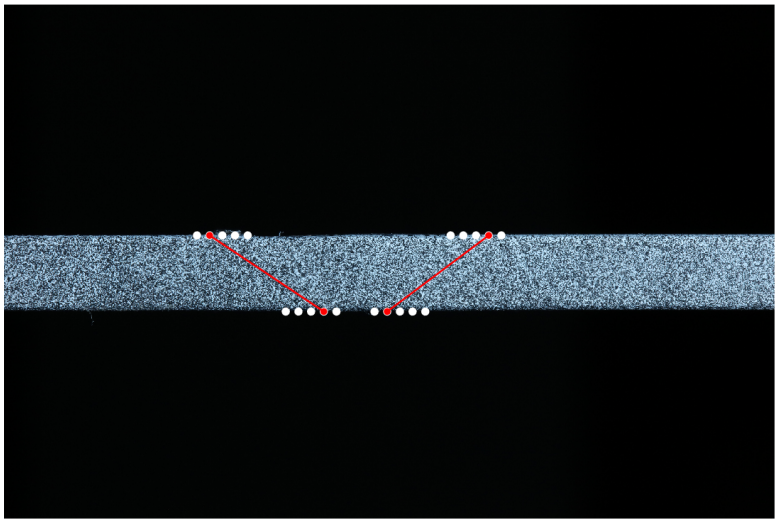

Figure 5.9: Typical optimization result of the location for the 4 points

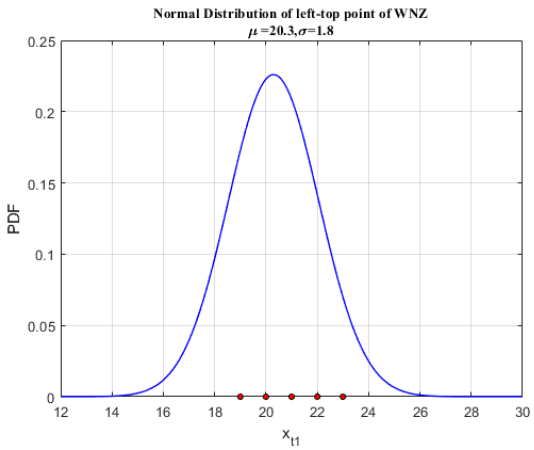

Figure 5.10: Normal distribution of the optimization result for x_{t1}

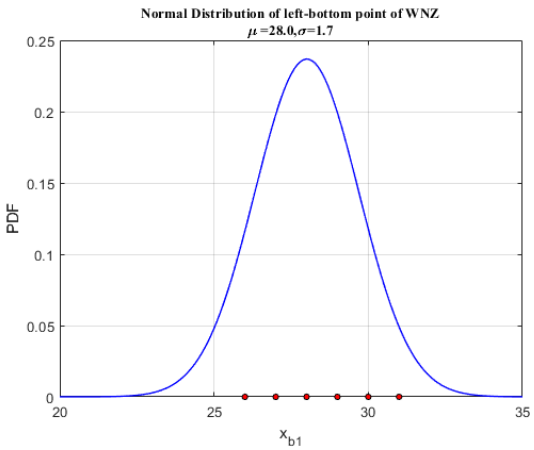

Figure 5.11: Normal distribution of the optimization result for x_{b1}

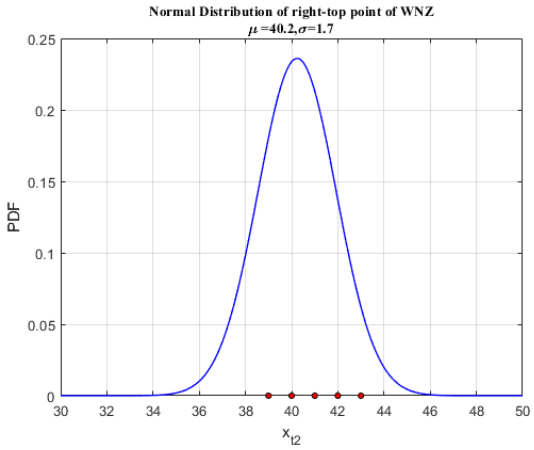

Figure 5.12: Normal distribution of the optimization result for x_{t2}

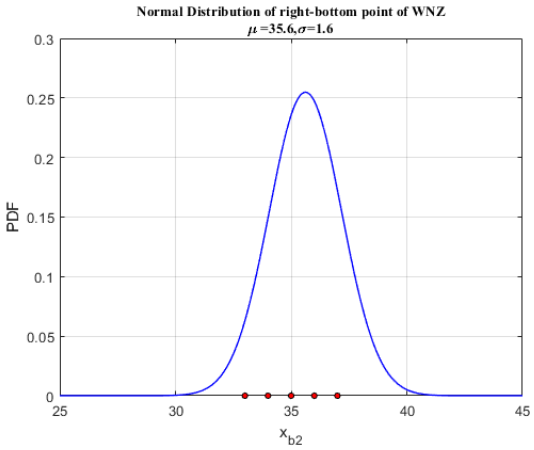

Figure 5.13: Normal distribution of the optimization result for x_{b2}

With the calculated mean value of the 4 variables, the ultimate optimization result of the point locations can be drawn on the DIC image displaying the boundary lines of material regions where actual properties differ.

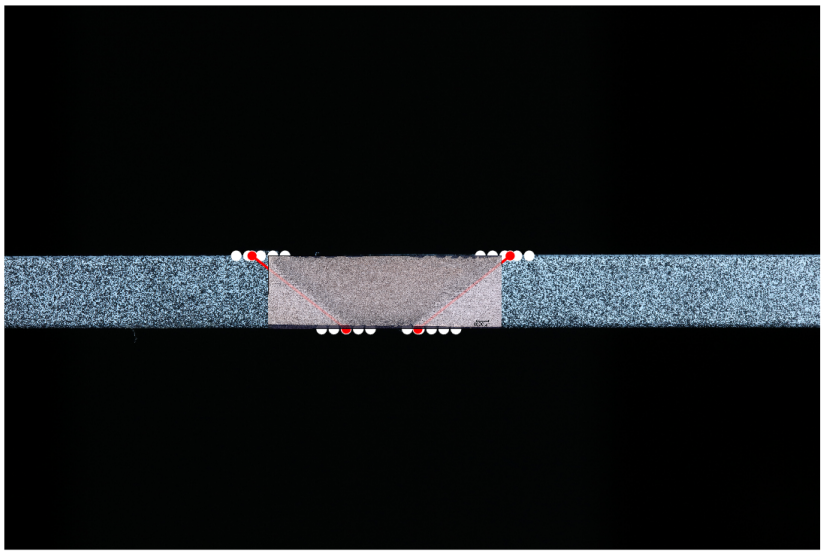

Figure 5.14: Final optimization result of the WNZ boundary lines

Finally, after post-processing, the most likely location of the WNZ boundary lines can be determined. Through a visual comparison with the original photo of the etched cross-section, it can be found that the actual calculated bottom width of WNZ is slightly larger than the visual width shown in the picture, while the top position is relatively offset to the left. These are all the concerns of the simplified model employed in this thesis.
It shall be noted that the Brutal Force method employed in this research has several drawbacks. Firstly, the optimization of the variables was not implemented in one step, i.e. optimizing $E_{BMZ}, E_{WNZ}, x_{t1}, x_{b1}, x_{t2}, x_{b2}$ simultaneously. The reason for not doing that was the unrealistic computational effort, which may take time up to 20 hours for one single operation. And the operation shall be repeated for 105 times. However, performing it in two steps introduces some potential issues. For instance, the nugget zone boundary lines are actually in different positions in the reference images and the deformed images, whereas in my approach, all calculations are based solely on the reference image. Although the dimension of the location deviation from the deformation of the structure itself is relatively small (around $0.1[mm]$ under the load of $400[MPa]$) compared to the search domain (around $10[mm]$), this method shows a systematic inaccuracy. Secondly, the search domain was proven to be not wide enough that in some rounds of optimization, the solutions were located at the boundaries. It is recommended to widen the search area and place more discrete solution points. In fact, without the help of a microscope for microscopic distinction, it is difficult to accurately divide the material region by simply analyzing the elastic properties of the structure through DIC or FEM methods. Several researches have been done trying to locate the boundary lines more precisely using methods such as microhardness test [35][36] and ultrasonic weld-guided waves[37]. Research is also done investigating the residual stress [38], which will have influence on the measurement of mechanical properties. It is recommended that in future studies if more detailed partitions of the material zones are required, this methodology can be tried to give a more precise measurement.

5.2. Parameter confidence

With the locations of boundary lines determined DIC measurement can be performed further. At constant intervals, the images of the specimen surfaces were taken. Based on these images DIC algorithm is able to generate full-field results for displacement U_x, U_y and strain $\epsilon_{xx}, \epsilon_{yy}, \epsilon_{xy}$, etc. The basic idea of calculating strain from the displacement field is to subtract rigid body motion first and set the length of ROI as the new structure length. With the strain data at axial and lateral directions in each loading condition Young's modulus and Poison's ratio can be calculated.

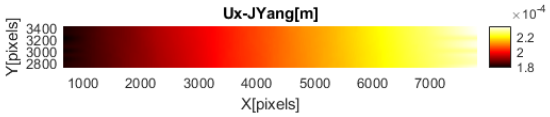

Figure 5.15: Typical displacement field U_x on ROI with rigid body motion

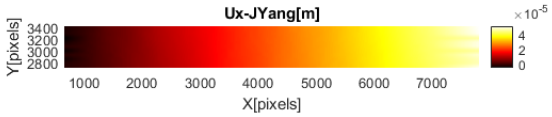

Figure 5.16: Typical displacement field U_x on ROI without rigid body motion

5.2.1. Young's modulus

Here two methods were applied to calculate Young's modulus. The first is to use the normal distribution. For each group of the DIC test, Young's modulus can be obtained by dividing the respective stress by the mean value of strain on the specified material zone. Another way of obtaining Young's modulus is by plotting the stress-strain curve and getting the slope of linear regression fitting.

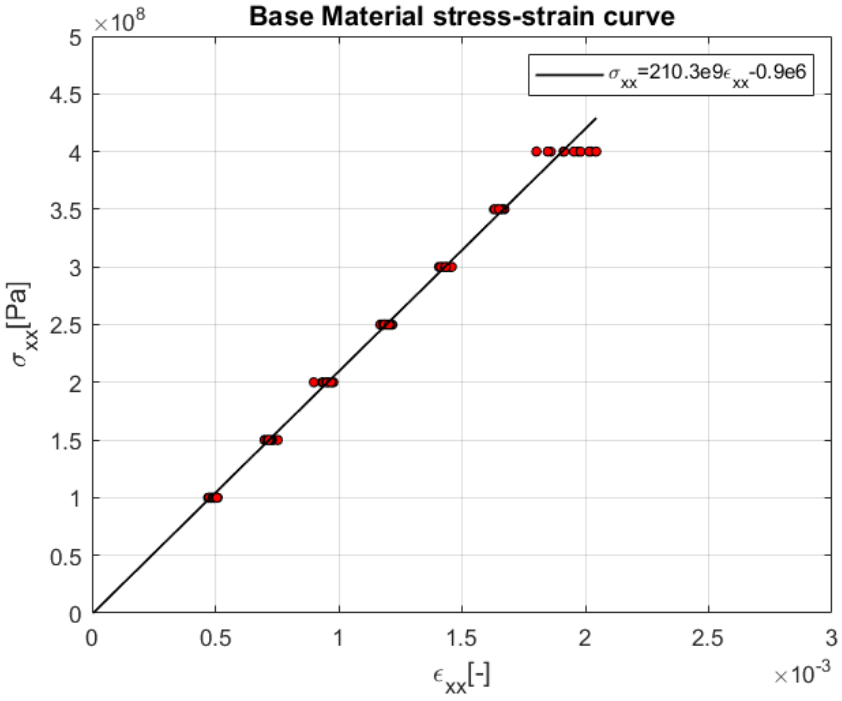

Figure 5.17: Stress-strain curve of BMZ

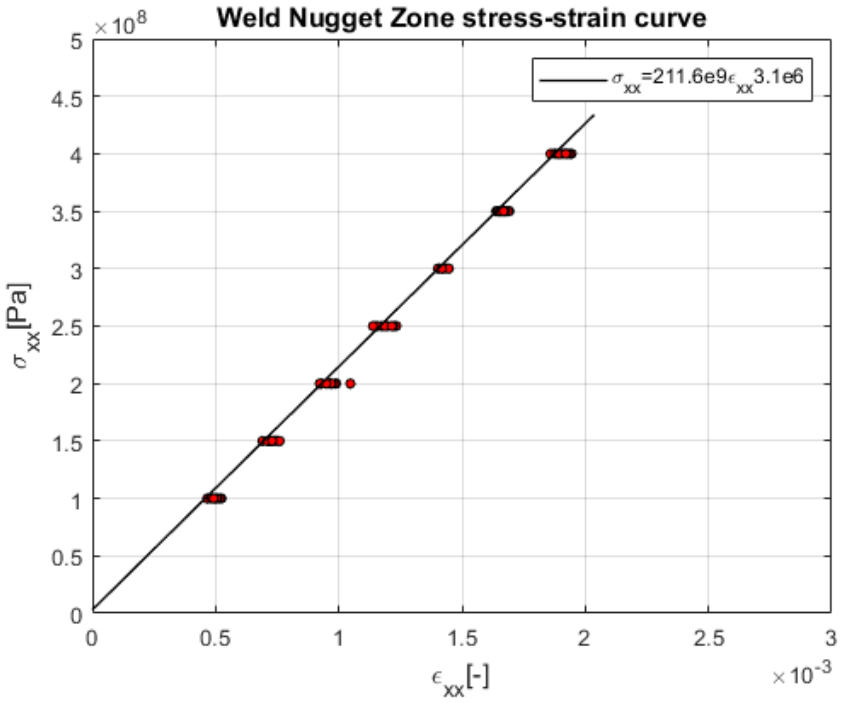

Figure 5.18: Stress-strain curve of WNZ

Figure 5.17 to 5.18 shows the stress-strain curve for the specified material zones. The base material, in this case, is S460 steel, which in the standard of Eurocode [39] has a Young's modulus of around $210GPa$. The fitting results are in line with this value.

Besides, up to the stress of $400MPa$, it can be found that the range of random variation for the BMZ (both left and the right-hand side) is larger, while for WNZ is not the case. Combined with the phenomena observed in the previous texture quality analysis, it is speculated that the BMZ material has slight plastic deformation at this level while the material in WNZ does not. It might be a signal that Friction Stir Welding can improve the axial strength of the steel material.

Usually, the fitting line of the stress-strain data should pass through the origin of the coordinates. In this case, there is little offset appearing which appears to be about 4% of the lowest stress load which can be regarded as negligible.

Figure 5.19 to 5.20 gives the normal distribution of Young's modulus for the specified material zones. Generally, Young's modulus computed through this method is slightly lower than that by linear fitting which might come from the offset from the coordinate origin.

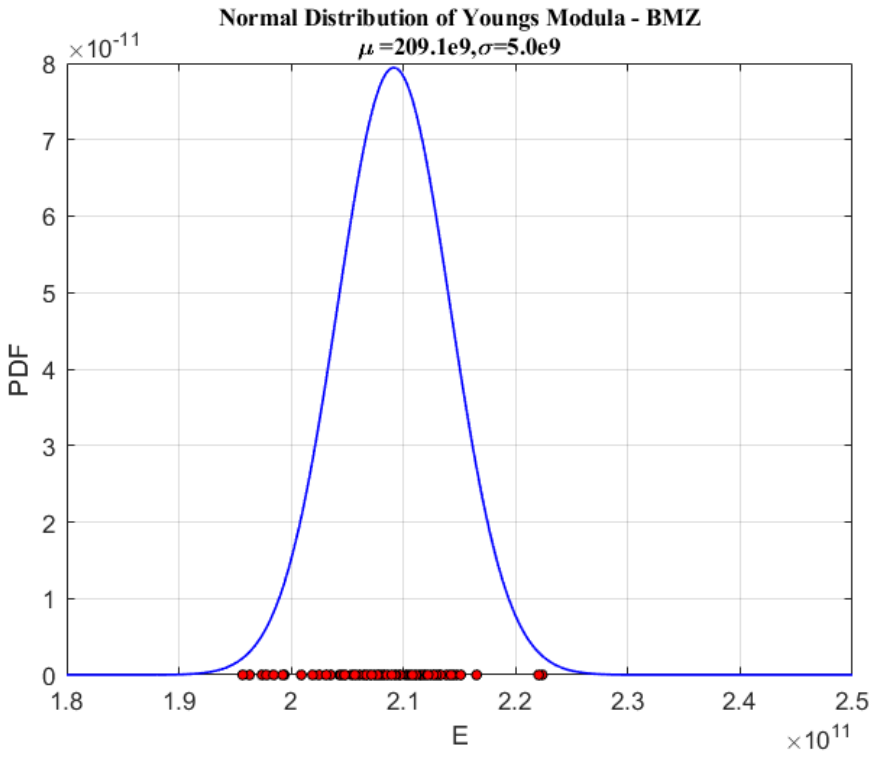

Figure 5.19: Normal Distribution of Young's Modulus of BMZ

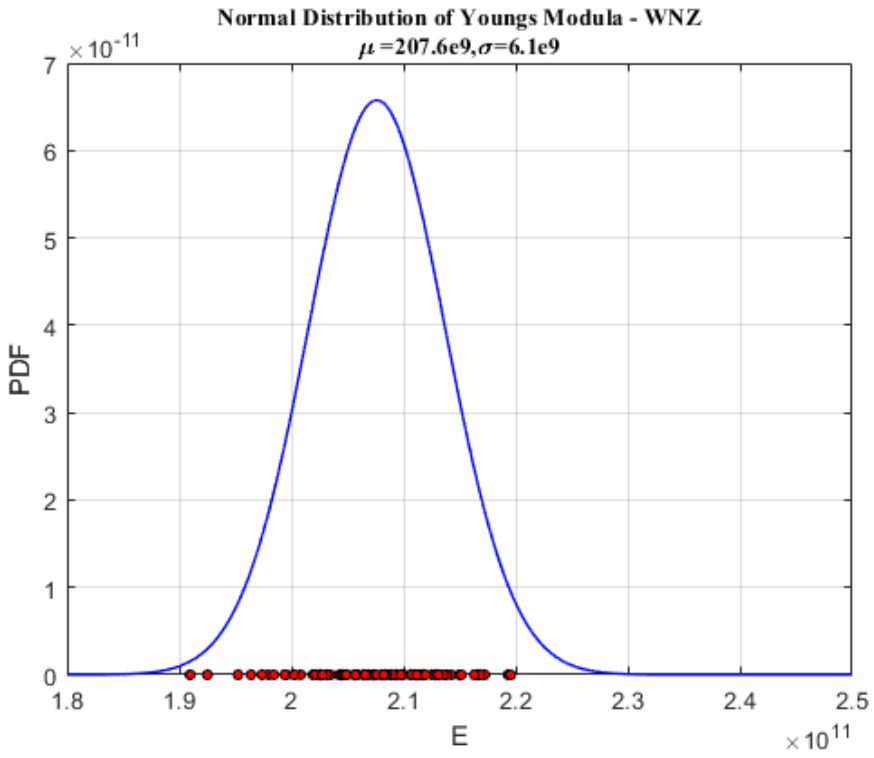

Figure 5.20: Normal Distribution of Young's Modulus of WNZ

5.2.2. Poisson's ratio

Poisson's ratio for the structure can be computed by plotting lateral strain vs. axial strains. By fitting the data points with a linear least square Poisson's ratio can be determined as the slope of fitting line[40].

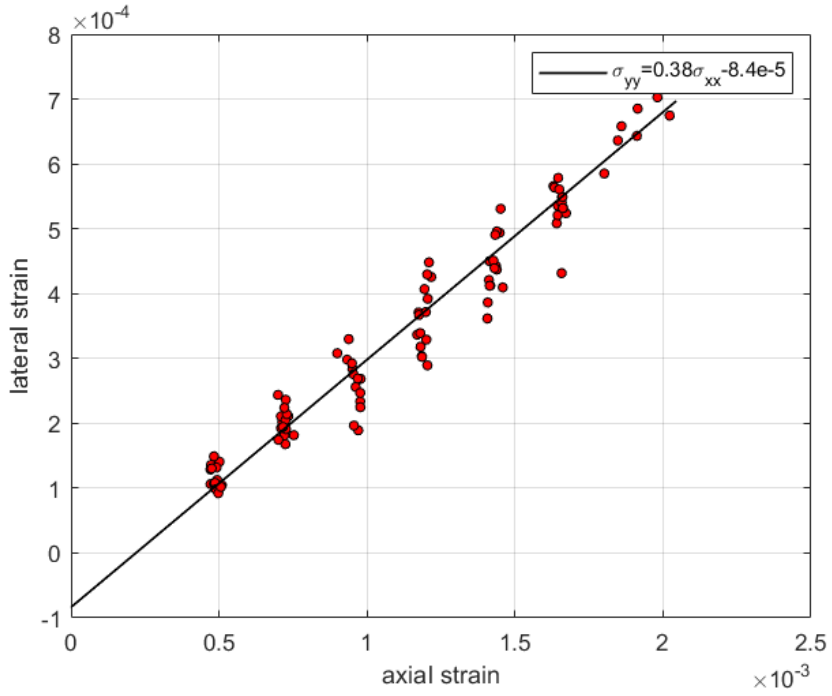

Figure 5.21: Lateral Strain vs. Axial Strain of BMZ

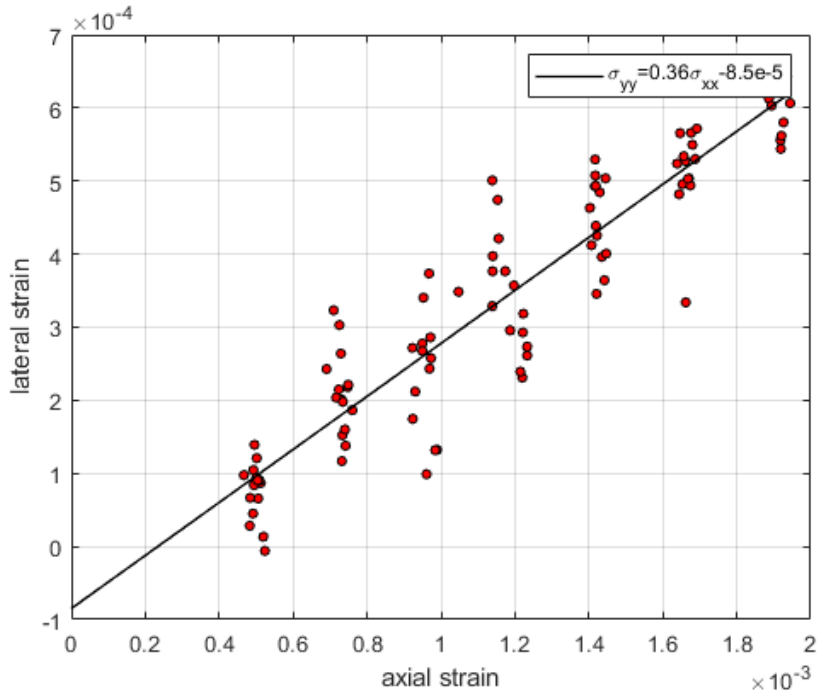

Figure 5.22: Lateral Strain vs. Axial Strain of WNZ

Figure 5.21 to 5.22 describes the relationship between lateral and axial strain for each material zone. However,

it can be observed that the fitting curve does not pass through the origin of coordinates and the distribution of data points is highly random. It's believed that applying a similar scheme, using the normal distribution to give a confidence bound of the parameter is more convincing.

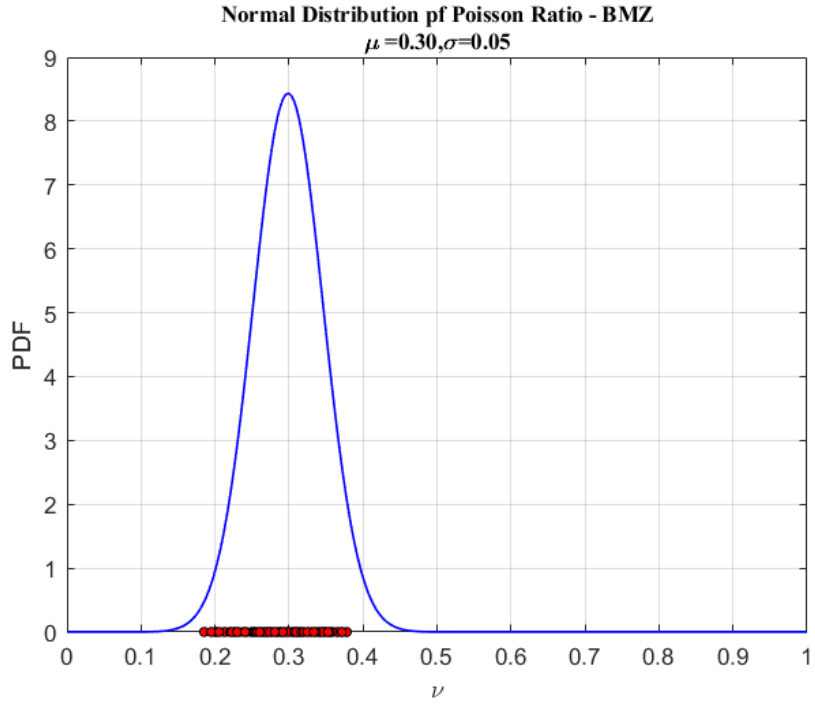

Figure 5.23: Normal distribution Poisson's ratio for BMZ

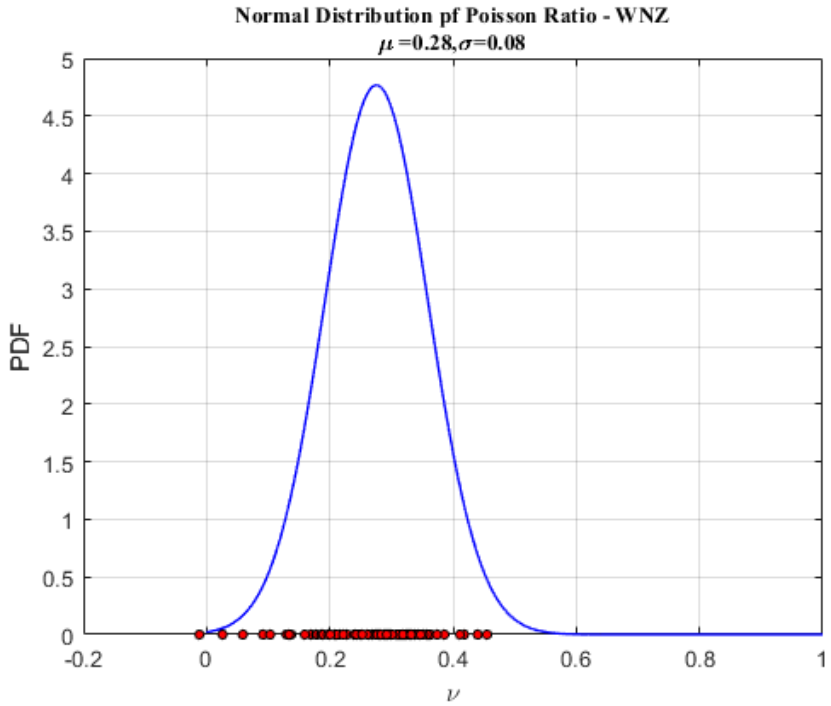

Figure 5.24: Normal distribution Poisson's ratio for WNZ

5.3. Concluding Remarks

Based on the results above, the measured elastic mechanical behaviors are as shown in Table 5.1 below.

Material Zone	Young's modulus[GPa]	Poisson's ratio[$-$]	Shear modulus[GPa]
BMZ	209.1	0.30	80.4
WNZ	207.6	0.28	81.4
Reference	210.0	0.30	81.0

Table 5.1: Elastic mechanical properties for the specified material zones

The following conclusions can be drawn from the measurement procedures and results in this chapter:

1. For the detection of material zone boundary lines a methodology is applied in this thesis that optimizes the difference between DIC and FEM results. This method works only for a simple partition of the material zones. For a detailed partition, the microscopic crystal nucleation changes can be adopted as a more convincing reference.

2. For the measurement of Young's modulus and Poisson's ratio, both linear regression fitting and normal distribution method are employed. In the case of Young's modulus, the result generated by the two methods varies a little. However, for Poisson's ratio. the first method of linear fitting is less convincing for the higher stochasticity of the data. The ultimate result is generally in line with the reference value in the case of the base material.

3. Through the stress-strain curve it can be observed that up to 400[MPa] there is obvious plastic behavior happening for BMZ while for WNZ the plastic behavior is not so evident. It can be regarded as an implication that FSW could improve the strength of the steel over base material.

6

Discussion and Future Outlook

6.1. Research questions

By this point, the 3 sub-questions outlined in Chapter 1 have been addressed:

- **Sub-question 1**: Which DIC formulation is best suited to capture accurate and robust displacement and strain field description at an acceptable computational test?
  A: According to the literature study, DIC formulations can be divided into 2 general categories: Global DIC method and Local DIC method. The global method usually uses self-defined finite element mesh as input. Theoretically, global DIC could directly establish the comparison between experimental results and numerical simulation results, hence minimalizing the discretization error. However, in practice, it's found that during the process of applying finite element mesh into DIC, some procedures like unit conversion(Global DIC method requires pixels as mesh units while FEM uses meters or millimeters) and the positioning of ROI in the images would introduce additional systematic errors.
  Local DIC usually exhibit better precision along with higher efficiency. For some material with inhomogeneous properties like FSW joints in this case, local DIC can also improve the smoothness of the result displacement and strain field.
  As a result, local DIC formulation is chosen to capture the displacement and strain field of the specimen.

- **Sub-question 2**: How to capture the elastic mechanical properties using Digital Image Correlation?
  A: Digital Image Correlation can only measure the displacement of a certain area by comparing the current image and reference image. For the measurement of static strength properties, both strain and stress data are required. There are 2 methods applicable in this case. The irst is to assume that the applied stress loading is along the longitudinal direction and evenly distributed in the cross-section area. According to the definition of Young's Modulus in the elastic region, by dividing the stress (as a constant value) over the stress field Young's modulus value of each finite element node could be obtained. The most likely value of Young's modulus can be determined by a chosen confidence interval.
  The other method is by the interaction of DIC and FEM results. Using the value of Young's Modulus of each material region as an input to the FEM analysis, by comparing the displacement field of DIC and FEM analysis after subtracting rigid body motion an optimum value could be obtained. This method is applicable based on that the material region boundary has been decided.

- **Sub-question 3**: How to partition the FSW joint material zones to capture the elastic mechanical properties for each one of them?
  A: There are several methods to partition the FSW joint material zones. In previous studies, methods such as microscope detecting or hardness tests have been put into use. During this thesis, with both DIC and FEM analysis available, a novel method is proposed that by setting the location and angle of the material zone boundary lines as variables, the partition problem can be modeled as an optimization problem. By optimizing the sum of the squared difference between the displacement or strain field of the DIC and FEM test over the chosen parameters, the most likely material boundary lines can be located.

However, there is still work to be done which is expected at the beginning of the thesis. In this chapter, the whole research will be reviewed through both the methodology and result to give an overview of the thesis work.

6.2. Experiment Setup

In this thesis in total 105 groups of data are to be analyzed by DIC, which has been proven to be enough to establish the confidence bound. The loading speed is set as $21[kN/s]$, which is within the limitation.

For the FEM modeling in this thesis, a 2D model with element type **Plane182** is employed. In the case of the measurement of deformation in the longitudinal direction, it can generate convincing results. However, if trying to coordinate the deformation simulated in the lateral direction, the deviation between FEM and DIC results is too large. (Figure 4.32 to Figure 4.35). To interpret the large deviation some speculations were made:

1. There exists a slight tilt in the recording camera and rigid body motion is not perfectly subtracted. Rigid body motion includes translational and rotational parts. During this thesis, the strategy of subtracting translational rigid body motion was to keep certain points (usually the left-end side points which are clamped at all the directions in ANSYS modeling) fixed which means no displacement is expected at them. Then take the derivative of the DIC displacement measurement result on the coordinates of the points and integrate them after resetting initial values (at the fixed points) to zero. To deal with rotational rigid body motion, a basic assumption was made that the whole ROI rotates at the same angle. So by comparing the displacement between the fixed point and its neighbor point this fixed angle can be determined. By operating matrix transformation on the displacement result inversely the rotational rigid body motion can be removed. The potential drawback of this method is that this fixed angle may depend on the choice of target nodes, which means a confidence interval of the rigid body rotational angle is present which was missing in the research process. Another idea of subtracting rotational rigid body motion is to transform the Cartesian coordinate system into a polar coordinate system. This method failed to be completed successfully.

2. The influence of 2-D FEM modeling. In this thesis, a Plane182 element was applied which is based on the assumption of "plane stress with thickness", which means that some out-of-plane deformations can not be detected through DIC. Although it can be imagined the out-of-plane effect would be relatively small compared with the behavior in other directions, it's recommended that in the future both 3D models can be established for FEM and 3D DIC can be adopted.

3. The FEM modeling of the specimen is incomplete. Only the region of interest in the DIC test was modeled in ANSYS, which means that the constraints were applied to the left-end side of the FEM model while in practice it should be on the shoulder. The deviation on the constraint point would make the FEM exhibit a higher displacement in the y direction.

As for the settings of DIC, in measuring the static behaviors of steel a subset size (or window size) of $32[pixels]$ is proven to be enough for capturing full-field displacement and strain. Each time a DIC analysis is to be carried out the texture quality evaluation should be implemented in priori.

6.3. DIC algorithm

2 different DIC algorithms were tried in this thesis while for ALDIC 2 different mesh types were gone through. The result has revealed that **ALDIC**, which functions as a global DIC, outperforms **RG-DIC** in both accuracy and robustness. In the case of ALDIC, it allows external input of FEM mesh. During the thesis, it has been verified that by using a trapezoid Q4 mesh rather than rectangular the computational accuracy and robustness to noise can be improved.

For the settings of ALDIC, it's recommended that FDM, rather than FEM, shall be employed to calculate the strain field. At least in measuring the elastic behavior FDM has shown better robustness to the noise data. Since in this case, 2D elastic behavior is to be analyzed, there is no difference in the strain field description with different theories. However, in future, if DIC is to be applied in measuring the plastic (which is non-linear) behavior, it can be speculated that infinitesimal strain theory would lose the accuracy. By then

Eulerian strain theory and Green-lagrangian theory should be compared.

In measuring the deformation DIC has been proved to be applicable in this case study. However, the influence of noise data and potentially the out-of-plane effects still exist. Also, the computational effort, especially when processing multiple images simultaneously and coordinating with FEM, is relatively high.

In the case of the comparison between DIC and FEM results, a Brutal Force method was applied which has several potential drawbacks:

1. Firstly, the optimization problem was not solved in one step. In the thesis, to save the computational effort, the six variables to be optimized are divided into 2 groups and optimized independently. This method is not rigorous in engineering research because the coupling relation between the variables is not taken into full consideration. Although to compensate for that an iterative step was added to the optimization procedure, the results remain unconvincing.

2. Secondly, the weld nugget zone boundaries have confidence bounds themselves. As shown in Figure 5.14, a qualitative comparison between the optimization result and etched photo was provided. However, it shall be noted that the background picture here is only representative of the reference images. For deformed images, the relative position of the weld nugget zone would shift, which was neglected during the optimization procedure. This drawback can also be addressed by combining the two steps of the Brutal Force method into one so that the 6 DoF optimization was operated independently for each picture.

3. Last, the Brutal Force method itself is not a real optimization algorithm. Because in this thesis FEM and DIC test was implemented in different software, I didn't manage to model the question into a real optimization problem. For the brutal force method that I applied, there are many solutions that fall on the edge of my preset domain, which would undoubtedly result in inaccuracy. An ideal way to address this problem was to complete the FEM analysis and DIC measurement in the same software and carry out the optimization using the built-in functions.

6.4. Mechanical properties

For Friction Stir Welded joints, the material zone partition can be complex and highly detailed, according to the micro-description of the grain shape and size. Simply comparing Young's modulus or other elastic properties is not sufficient to capture a more detailed partition. It is recommended that in future work micro-indentation tests or methods like ultrasonic weld-guided waves can be adopted.

As for the measurement itself, there was an interesting observation that up to the load level of 400$[MPa]$, the randomness of stress-strain points significantly increased in the BMZ but not in the WNZ. This might be an implication of plastic behavior. Based on this finding it can be speculated that up to such load level, the base material has already exhibited plastic behavior while the weld nugget material has not. It might be a signal that Friction Stir Welding is able to improve the axial strength of the steel material. In future studies, this can be further investigated by either a detailed partitional of the material zone or by the measurement of plastic properties applying DIC. And other mechanical properties including Yield Strength and Ultimate Strength can expected for each material zone.

Besides, during the determination of Poisson's ratio, the result exhibits high stochasticity between different deformed images. I haven't found a reasonable explanation for this phenomenon yet but it can be sure to be in the part of strain calculation in the DIC algorithm. Because up to the step of displacement measurement in the y direction, the selection of deformed images does not show much deviation. The incomplete subtraction of rotational rigid body motion may also play a significant role in this problem.

Finally, in this thesis, the study is restricted only to the static performance of the structure, and for the static performance, only the properties in the elastic region are measured. DIC has been proven to be a convincing tool that can be applied in the future to calculate properties like Yield strength and Ultimate strength. Fatigue information of the structure can also be considered to be evaluated by DIC for FSW joints in the future.

Bibliography

[1] Mukuna Patrick Mubiayi, Esther Titilayo Akinlabi, and Mamookho Elizabeth Makhatha. *Current trends in friction stir welding (FSW) and friction stir spot welding (FSSW)*. Vol. 6. Springer, 2019.

[2] ir.N.C.H.Troost. *MTT Colloquium presentation: Underwater Friction Stir Welding*.

[3] Anthony P Reynolds et al. "Structure, properties, and residual stress of 304L stainless steel friction stir welds". In: *Scripta materialia* 48.9 (2003), pp. 1289–1294.

[4] Anthony P Reynolds, WD Lockwood, and TU Seidel. "Processing-property correlation in friction stir welds". In: *Materials science forum*. Vol. 331. Trans Tech Publ. 2000, pp. 1719–1724.

[5] *Standard Test Methods and Definitions for Mechanical Testing of Steel Products*. Standard. American Society for Testing and Materials International, 2022.

[6] Devan Atkinson and Thorsten Becker. "A 117 Line 2D Digital Image Correlation Code Written in MATLAB". In: *Remote Sensing* 12 (Sept. 2020), p. 2906. DOI: 10.3390/rs12182906.

[7] François Hild and Stéphane Roux. "CorreliQ4: A software for finite element displacement field measurements by digital image correlation". In: *Rapport interne LMT Cachan* 269 (2008), p. 195.

[8] Stéphane Roux, Julien Réthoré, and François Hild. "Digital image correlation and fracture: an advanced technique for estimating stress intensity factors of 2D and 3D cracks". In: *Journal of Physics D: Applied Physics* 42.21 (2009), p. 214004.

[9] Peng Cheng et al. "Full-field speckle pattern image correlation with B-spline deformation function". In: *Experimental mechanics* 42 (2002), pp. 344–352.

[10] Abraham Savitzky and Marcel JE Golay. "Smoothing and differentiation of data by simplified least squares procedures." In: *Analytical chemistry* 36.8 (1964), pp. 1627–1639.

[11] JH Den Besten. "Fatigue resistance of welded joints in aluminium high-speed craft: a total stress concept". In: (2015).

[12] Jin Yang and Kaushik Bhattacharya. "Augmented Lagrangian Digital Image Correlation". In: *Experimental Mechanics* (Dec. 2018). DOI: 10.1007/s11340-018-00457-0.

[13] Jin Yang and Kaushik Bhattacharya. "Combining Image Compression with Digital Image Correlation". In: *Experimental Mechanics* (Jan. 2019). DOI: 10.1007/s11340-018-00459-y.

[14] J Blaber, B Adair, and A Antoniou. "Ncorr: open-source 2D digital image correlation matlab software". In: *Experimental Mechanics* 55.6 (2015), pp. 1105–1122.

[15] Devan Atkinson and Thorsten Becker. "A 117 Line 2D Digital Image Correlation Code Written in MATLAB". In: *Remote Sensing* 12 (Sept. 2020), p. 2906. DOI: 10.3390/rs12182906.

[16] Bo Wang and Bing Pan. "Subset-based local vs. finite element-based global digital image correlation: A comparison study". In: *Theoretical and Applied Mechanics Letters* 6.5 (2016), pp. 200–208. ISSN: 2095-0349. DOI: https://doi.org/10.1016/j.taml.2016.08.003. URL: https://www.sciencedirect.com/science/article/pii/S2095034916300411.

[17] B Pan, K Li, and W Tong. "Fast, robust and accurate digital image correlation calculation without redundant computations". In: *Experimental Mechanics* 53.7 (2013), pp. 1277–1289.

[18] Bing Pan. "Reliability-guided digital image correlation for image deformation measurement". In: *Applied optics* 48.8 (2009), pp. 1535–1542.

[19] H Lu and PD Cary. "Deformation measurements by digital image correlation: Implementation of a second-order displacement gradient". In: *Experimental mechanics* 40.4 (2000), pp. 393–400.

[20] Justin Blaber. *Ncorr DIC algorithm*. http://www.ncorr.com/index.php.

[21] Bing Pan et al. “Digital image correlation using iterative least squares and pointwise least squares for displacement field and strain field measurements”. In: *Optics and Lasers in Engineering* 47.7 (2009), pp. 865–874. ISSN: 0143-8166. DOI: https://doi.org/10.1016/j.optlaseng.2008.10.014. URL: https://www.sciencedirect.com/science/article/pii/S0143816609000189.

[22] Jia-qing Zhao et al. “Improved Hermite finite element smoothing method for full-field strain measurement over arbitrary region of interest in digital image correlation”. In: *Optics and Lasers in Engineering* 50.11 (2012), pp. 1662–1671. ISSN: 0143-8166. DOI: https://doi.org/10.1016/j.optlaseng.2012.04.008. URL: https://www.sciencedirect.com/science/article/pii/S0143816612001236.

[23] Stéphane Avril et al. “Comparison of two approaches for differentiating full-field data in solid mechanics”. In: *Measurement Science and Technology* 21.1 (Dec. 2009), p. 015703. DOI: 10.1088/0957-0233/21/1/015703. URL: https://dx.doi.org/10.1088/0957-0233/21/1/015703.

[24] Jeffrey D. Helm, Stephen R. McNeill, and Michael A. Sutton. “Improved three-dimensional image correlation for surface displacement measurement”. In: *Optical Engineering* 35.7 (1996), pp. 1911–1920. DOI: 10.1117/1.600624. URL: https://doi.org/10.1117/1.600624.

[25] M.A. Sutton et al. “The effect of out-of-plane motion on 2D and 3D digital image correlation measurements”. In: *Optics and Lasers in Engineering* 46.10 (2008), pp. 746–757. ISSN: 0143-8166. DOI: https://doi.org/10.1016/j.optlaseng.2008.05.005. URL: https://www.sciencedirect.com/science/article/pii/S0143816608000985.

[26] Frederik Michel Dekking et al. *A Modern Introduction to Probability and Statistics: Understanding why and how*. Vol. 488. Springer, 2005.

[27] Sandra Bergonnier, François Hild, and Stéphane Roux. “Local anisotropy analysis for non-smooth images”. In: *Pattern recognition* 40.2 (2007), pp. 544–556.

[28] T. Liszka and J. Orkisz. “The finite difference method at arbitrary irregular grids and its application in applied mechanics”. In: *Computers & Structures* 11.1 (1980). Special Issue-Computational Methods in Nonlinear Mechanics, pp. 83–95. ISSN: 0045-7949.

[29] John O Dow, Michael S Jones, and Shawn A Harwood. “A new approach to boundary modelling for finite difference applications in solid mechanics”. In: *International Journal for Numerical Methods in Engineering* 30.1 (1990), pp. 99–113.

[30] Yaofeng Sun et al. “Finite element formulation for a digital image correlation method”. In: *Applied optics* 44.34 (2005), pp. 7357–7363.

[31] Gilles Besnard, François Hild, and Stéphane Roux. ““Finite-element” displacement fields analysis from digital images: application to Portevin–Le Châtelier bands”. In: *Experimental mechanics* 46 (2006), pp. 789–803.

[32] Stéphane Avril et al. “Comparison of two approaches for differentiating full-field data in solid mechanics”. In: *Measurement Science and Technology* 21.1 (2009), p. 015703.

[33] Ted Belytschko et al. *Nonlinear finite elements for continua and structures*. John wiley & sons, 2014.

[34] Dr Majeed, Yashwant Mehta, and Arshad Siddiquee. “Precipitation-Dependent Corrosion Analysis of Heat Treatable Aluminum Alloys via Friction Stir Welding, a Review”. In: *Proceedings of the Institution of Mechanical Engineers, Part C: Journal of Mechanical Engineering Science* 235 (Feb. 2021). DOI: 10.1177/09544062211003609.

[35] Raju Prasad Mahto and Surjya Kanta Pal. “Friction stir welding of dissimilar materials: an investigation of microstructure and nano-indentation study”. In: *Journal of Manufacturing Processes* 55 (2020), pp. 103–118.

[36] M Cabibbo et al. “Double side friction stir welding of AA6082 sheets: Microstructure and nanoindentation characterization”. In: *Materials Science and Engineering: A* 590 (2014), pp. 209–217.

[37] Yishou Wang et al. “Propagation characteristics of ultrasonic weld-guided waves in friction stir welding joint of same material”. In: *Ultrasonics* 102 (2020), p. 106058.

[38] Michael B Prime et al. “Residual stress measurements in a thick, dissimilar aluminum alloy friction stir weld”. In: *Acta materialia* 54.15 (2006), pp. 4013–4021.

[39] *Eurocode 3: design of steel structures : part 1-5 : plated structural elements*. Incorporating corrigendum April 2009. London: BSI, 2010. URL: https://cds.cern.ch/record/1701996.

[40] Fawad Tariq et al. “Application of Digital Image Correlation Technique in determination of elastic constants of materials”. In: Feb. 2012.

[41] Brilliant.org. *Newton Raphson Method*. `https://brilliant.org/wiki/newton-raphson-method/`. 2023.

[42] Jean-Charles Passieux and Robin Bouclier. “Classic and inverse compositional Gauss-Newton in global DIC”. In: *International Journal for Numerical Methods in Engineering* 119.6 (2019), pp. 453–468.

A

Optimization algorithm

A.1. Newton-Raphson Method

Newton-Raphson(NR) Method is an approximation method to find the root of the valued function $f(x) = 0$, the key idea is to approximate a continuous and differentiable function with a straight line tangent to the function.

NR method begins with an assigned point $x = x_n$, followed by a primary function with a slope of $f'(x_n)$, by setting $y = 0$ the new approximation root was found as $x_{n+1} = x_n - \frac{f(x_n)}{f'(x_n)}$. This iteration procedure will be performed several times until an assigned minimum tolerance is reached.

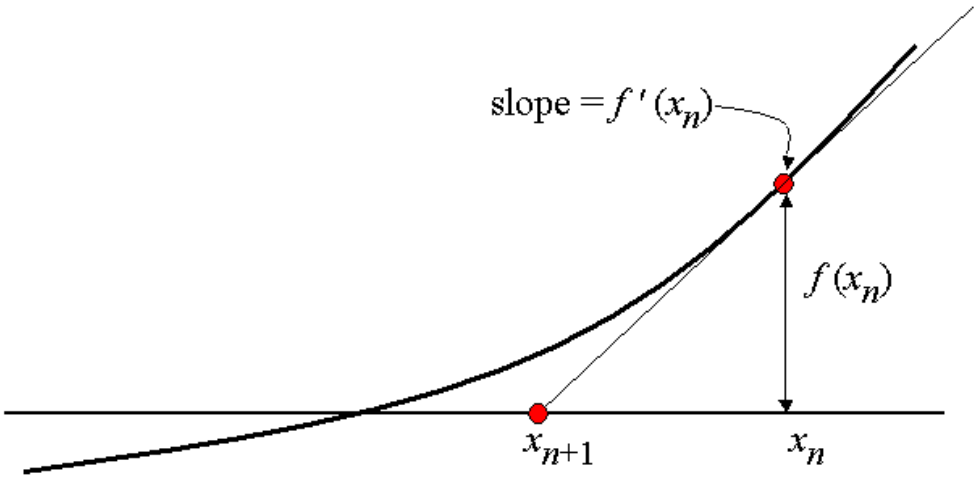

Figure A.1: Illustration of Newton's method[41]

As a conventional estimated solution-finding method, NR method has several limitations such as failure in case of $f'(x_0) = 0$ or where there are points of inflection, local maxima or minima.

A.2. Inverse Compositional Gauss-Newton

There are several methods that can be adopted to solve the optimization described by the formula 2.15, among which inverse compositional gauss-newton(IC-GN) is the most commonly used one. The key idea of IC-GN is to linearize the minimization optimization problem in such a way that the use of Gauss-Newton naturally leads to a constant operator[42].
The aim of the IC-GN method in the DIC technique is to figure out the deformation map $\mathbf{y}^{k+1}$ with the given iteration step $\mathbf{y}^k$. For convenience we define the inverse map $\phi^k(\mathbf{y}^k(\mathbf{X})) = \mathbf{X}$ and the increment ψ^k where $\mathbf{y}^{k+1} = \mathbf{y}^k \circ \psi^k$. As a result

$$\phi^{k+1} = \phi^k \circ (\psi^k)^{-1} \tag{A.1}$$

Here first-order approximation is applied:

$$\psi^k \approx \mathbf{z} + \mathbf{v} + \mathbf{H}(\mathbf{z} - \mathbf{z}_0) \tag{A.2}$$

Where $\mathbf{z} = \mathbf{y}^k$,

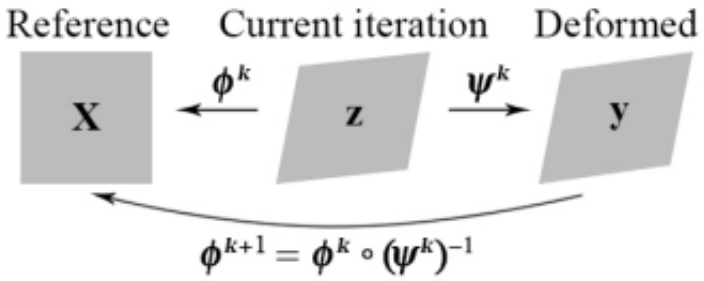

Figure A.2: Variable mapping in IC-GN method

B

Matlab-ANSYS interaction code

In this thesis, interaction between MATLAB and ANSYS is required to compare the FEM and DIC result. The technical solution to that is to use Matlab to batch generate and run ANSYS files. Appendix B has listed the Matlab codes used to complete the interaction and post-processing (the Brutal Force Method). An example ansys file is required for each run.

```
% Initialization
clearvars
clc
format compact

% Create folder route
ansFilesRoute="ansFiles\\";
simFilesRoute="SimOut\\";
resFilesRoute="ansResult\\";
ANSYS_dir='"D:\\ANSYS Inc\\v191\\ansys\\bin\\winx64\\ANSYS191.exe"';

exampleFileName = "FSW2D_trapeExample.ans";
textOrig = fileread(exampleFileName);

% Variable value list
BMZ_bList = [26.0 27.0 28.0 29.0 30.0];
BMZ_tList = [19.0 20.0 21.0 22.0 23.0];
WNZ_bList = [33.0 34.0 35.0 36.0 37.0];
WNZ_tList = [39.0 40.0 41.0 42.0 43.0];

for i = 1:size(BMZ_bList,2)
for j = 1:size(BMZ_tList,2)
for k = 1:size(WNZ_bList,2)
for m = 1:size(WNZ_tList,2)
    % make directorty
    mkdir('D:\Thesis Project\ANSYS analysis\ansResult',strcat('FSW2D_Result_',num2str(i),"_",↙
num2str(j),"_",num2str(k),"_",num2str(m))); %%% New folder created for ANSYS result files
    % change the texts in the ans file
    text = textOrig+"";
    text = strrep(text,"BMZ_bVal",num2str(BMZ_bList(i)));
    text = strrep(text,"BMZ_tVal",num2str(BMZ_tList(j)));
    text = strrep(text,"WNZ_bVal",num2str(WNZ_bList(k)));
    text = strrep(text,"WNZ_tVal",num2str(WNZ_tList(m)));
    text = strrep(text,"FolderVal",strcat('FSW2D_Result_',num2str(i),"_",num2str(j),"_",num2str↙
(k),"_",num2str(m)));

    outputFileName = strcat(...
        "FSW2D_trape_",num2str(i),"_",num2str(j),"_",num2str(k),"_",num2str(m),".ans" ...
    );
    fileID = fopen(ansFilesRoute+outputFileName,'w');
    fprintf(fileID,text);
    fclose(fileID);

    SimOutFileName = strcat(...
        "SimOut_",num2str(i),"_",num2str(j),"_",num2str(k),"_",num2str(m),".txt" ...
    );
    batchString = cell(1,1);
    batchString{1} = ...
```

```
        "SET KMP_STACKSIZE=70000k & " + ...
        ANSYS_dir +...
        " -b -i " + ansFilesRoute + outputFileName +" -o " + simFilesRoute + SimOutFileName;
    fileID = fopen("LAUNCH.BAT",'w');
    fprintf(fileID,batchString{1});
    fclose(fileID);

    [status,~]=dos('LAUNCH.BAT'); % Run ANSYS through dos
    delete file.lock file.page file.err file.log LAUNCH.BAT % Delete log files
end
end
end
end
```

```
%%%%%%%%%%%%%%%%%%%%%%%%%%%%%%%%%%%%%%%%%%%%%%%%%%%%%%%%%%%%%%%%%%%%%%%
%%% This matlab script is used to find the optimized %%%%
%%% boundary location of FSW by comparing FEM and DIC %%%
%%%%%%%%%%%%%%%%%%%%%%%%%%%%%%%%%%%%%%%%%%%%%%%%%%%%%%%%%%%%%%%%%%%%%%%

clear
clc
close all

%% DIC data
UnitRatio = 6e-3/780;
trap = load('results_FE_globalDIC_IMG_0281_0288_st32_alpha10.mat');
Ux_JYang = -trap.ResultStrainWorld{1,1}.dispu;
Uy_JYang = trap.ResultStrainWorld{1,1}.dispv;
% Resort the displacement field result in order of the World Coordinates (JYang)
% Coordinates FEM (Cartesian)
CarX = trap.DICmesh.coordinatesFEM(:,1);
CarY = trap.DICmesh.coordinatesFEM(:,2);

Cart = [CarX,CarY];
[Cart_sorted_x, SortIndex_x] = sortrows(Cart,[2,1]);% Sort the nodes 1st in order of X and 2nd in order of Y
Ux_sorted = Ux_JYang(SortIndex_x); % Sort Ux in order of above
Uy_sorted = Uy_JYang(SortIndex_x); % Sort Uy in order of above
Matrix_Ux = [SortIndex_x,Cart_sorted_x,Ux_sorted];

% Subtract Rigid Body Motion
Matrix_Ux(:,5) = Matrix_Ux(:,4)-min(Matrix_Ux(:,4));
% Matrix_Ux(:,6) = Uy_sorted-max(Uy_sorted);
Matrix_Ux(:,6) = Uy_sorted;
%Matrix_Ux(:,5) = Matrix_Ux(:,4);
% Resort into matrix according to the coordinates
Ux_JYang = reshape(Matrix_Ux(:,5),69,10);
% Interpolate it into local DIC mesh
F_Ux_JYang = scatteredInterpolant(Matrix_Ux(:,2),Matrix_Ux(:,3),Matrix_Ux(:,5),'linear');
F_Uy_JYang = scatteredInterpolant(Matrix_Ux(:,2),Matrix_Ux(:,3),Matrix_Ux(:,6),'linear');

% Reshape
Size_Ux = [37,376];
X1 = linspace(600,7000,Size_Ux(2));
Y1 = linspace(2700,3350,Size_Ux(1));
[X_plot,Y_plot] = meshgrid(X1,Y1);
UxPlot_JYang = F_Ux_JYang(X_plot,Y_plot).*UnitRatio;
UyPlot_JYang = F_Uy_JYang(X_plot,Y_plot).*UnitRatio;

%% FEM data
SSD_JYang_FEM = zeros(5,5,5,5);
Mean_JYang_FEM = zeros(5,5,5,5);
```

```
Std_JYang_FEM = zeros(5,5,5,5);

for i = 1:5
for j = 1:5
for k = 1:5
for m = 1:5
    % Path
    pathFolder = strcat('D:\Thesis Project\ANSYS analysis\ansResult\','FSW2D_Result_',num2str(i),"↙
_",num2str(j),"_",num2str(k),"_",num2str(m));
    pathDisp = strcat(pathFolder,'\DispXY.txt');
    pathCoor = strcat(pathFolder,'\Coordinate.txt');

    % Cooridinates
    fidOut=fopen(pathCoor,'r');
    Coordinate=fscanf(fidOut,'%f\n');
    fclose(fidOut);
    fidClear=fopen('Coordinate.txt','w');
    fprintf(fidClear,'%s',' ');
    fclose(fidClear);
    CoordinateXY=[Coordinate(1:2:end),Coordinate(2:2:end)];

    % Displacements
    fidOut=fopen(pathDisp,'r');
    DispXY=fscanf(fidOut,'%f\n');
    fclose(fidOut);
    fidClear=fopen('DispXY.txt','w');
    fprintf(fidClear,'%s',' ');
    fclose(fidClear);
    DispXY=[DispXY(1:2:end),DispXY(2:2:end)];

    Ux_FEM = DispXY(:,1);
    Uy_FEM = DispXY(:,2);
    Car_FEM = [CoordinateXY(:,1),CoordinateXY(:,2)]./UnitRatio;
    [Cart_sorted_x_FEM, SortIndex_x_FEM] = sortrows(Car_FEM,[2,1]);% Sort the nodes 1st in order↙
of X and 2nd in order of Y
    Ux_sorted_FEM = Ux_FEM(SortIndex_x_FEM); % Sort Ux in order of above
    Uy_sorted_FEM = Uy_FEM(SortIndex_x_FEM); % Sort Uy in order of above
    Matrix_Ux_FEM = [SortIndex_x_FEM,Cart_sorted_x_FEM,Ux_sorted_FEM,Uy_sorted_FEM];
    F_Ux_FEM = scatteredInterpolant(Matrix_Ux_FEM(:,2),Matrix_Ux_FEM(:,3),Ux_sorted_FEM,'linear');
    F_Uy_FEM = scatteredInterpolant(Matrix_Ux_FEM(:,2),Matrix_Ux_FEM(:,3),Uy_sorted_FEM,'linear');

    % Comparison
    UxPlot_FEM = F_Ux_FEM(X_plot,Y_plot);
    UyPlot_FEM = F_Uy_FEM(X_plot,Y_plot);

    SD_JYang_FEM = (UxPlot_JYang(:,100:276)-UxPlot_FEM(:,100:276)).^2;
    SSD_JYang_FEM(i,j,k,m) = sum(SD_JYang_FEM,'all');
    Mean_JYang_FEM(i,j,k,m) = mean(SD_JYang_FEM,'all');
```

```
    Std_JYang_FEM(i,j,k,m) = std(SD_JYang_FEM,0,'all');
end
end
end
end

%% Optimization

for i = 1:5
for j = 1:5
for k = 1:5
for m = 1:5
    if Mean_JYang_FEM(i,j,k,m) == min(min(min(min(Mean_JYang_FEM))))
        i_min = i;
        j_min = j;
        k_min = k;
        m_min = m;
    end
end
end
end
end

%% Plot
% [mm]
BMZ_bList = [26.0 27.0 28.0 29.0 30.0];
BMZ_tList = [19.0 20.0 21.0 22.0 23.0];
WNZ_bList = [33.0 34.0 35.0 36.0 37.0];
WNZ_tList = [39.0 40.0 41.0 42.0 43.0];

figure(1)
surf(BMZ_tList,WNZ_tList,Mean_JYang_FEM(:,:,1,1))
xlabel('x_{t1}[mm]');
ylabel('x_{t2}[mm]');

%% Plot on the original photo(reference image) to show the material boundary
% import specimen photo
Ht = 20.5e-3/UnitRatio;
Hb = 26.5e-3/UnitRatio;
X1 = (BMZ_bList(i_min)/1000)/UnitRatio;
X2 = (BMZ_tList(j_min)/1000)/UnitRatio;
X3 = (WNZ_bList(k_min)/1000)/UnitRatio;
X4 = (WNZ_tList(m_min)/1000)/UnitRatio;

Fig_fsw = imread('IMG_0030.JPG');
figure(2)
imshow(Fig_fsw)
hold on
```

```
for i = 1:5
    plot((BMZ_bList(i)/1000)/UnitRatio,Hb,'Linestyle','none','Marker','o',...
        'MarkerEdgeColor','White','MarkerFaceColor','White','MarkerSize',8')
end
for i = 1:5
    plot((BMZ_tList(i)/1000)/UnitRatio,Ht,'Linestyle','none','Marker','o',...
        'MarkerEdgeColor','White','MarkerFaceColor','White','MarkerSize',8')
end
for i = 1:5
    plot((WNZ_bList(i)/1000)/UnitRatio,Hb,'Linestyle','none','Marker','o',...
        'MarkerEdgeColor','White','MarkerFaceColor','White','MarkerSize',8')
end
for i = 1:5
    plot((WNZ_tList(i)/1000)/UnitRatio,Ht,'Linestyle','none','Marker','o',...
        'MarkerEdgeColor','White','MarkerFaceColor','White','MarkerSize',8')
end
plot(X1,Hb,'Linestyle','none','Marker','o',...
        'MarkerEdgeColor','White','MarkerFaceColor','Red','MarkerSize',8')
plot(X2,Ht,'Linestyle','none','Marker','o',...
        'MarkerEdgeColor','White','MarkerFaceColor','Red','MarkerSize',8')
plot(X3,Hb,'Linestyle','none','Marker','o',...
        'MarkerEdgeColor','White','MarkerFaceColor','Red','MarkerSize',8')
plot(X4,Ht,'Linestyle','none','Marker','o',...
        'MarkerEdgeColor','White','MarkerFaceColor','Red','MarkerSize',8')
plot([X1,X2],[Hb,Ht],'-r','Linewidth',2)
plot([X3,X4],[Hb,Ht],'-r','Linewidth',2)
```